AGU PUBLICATIONS

JGR

Journal of Geophysical Research: Space Physics

RESEARCH ARTICLE
10.1002/2016JA023770

Second harmonic poloidal waves observed by Van Allen Probes in the dusk-midnight sector

Kyungguk Min[1], Kazue Takahashi[1], Aleksandr Y. Ukhorskiy[1], Jerry W. Manweiler[2], Harlan E. Spence[3], Howard, J. Singer[4], Seth G. Claudepierre[5], Brian A. Larsen[6], A. Rualdo Soto-Chavez[7], and Ross J. Cohen[7]

[1]The Johns Hopkins University Applied Physics Laboratory, Laurel, Maryland, USA, [2]Fundamental Technologies, LLC, Lawrence, Kansas, USA, [3]Department of Physics, Institute for Earth, Oceans and Space, University of New Hampshire, Durham, New Hampshire, USA, [4]Space Weather Prediction Center, NOAA, Boulder, Colorado, USA, [5]Space Sciences Department, The Aerospace Corporation, El Segundo, California, USA, [6]Space Science and Applications Group, Los Alamos National Laboratory, Los Alamos, New Mexico, USA, [7]Center for Solar-Terrestrial Research, New Jersey Institute of Technology, Newark, New Jersey, USA

Key Points:
- Poloidal mode ULF waves near the premidnight sector during a quiet geomagnetic time
- Second harmonic, high *m* number poloidal mode at westward propagation likely driven by an inward radial gradient of ring current protons
- The background plasma density appears to be important for the longitudinal and radial extents of the wave active region

Correspondence to:
K. Min,
kyungguk.min@jhuapl.edu

Citation:
Min, K., K. Takahashi, A. Y. Ukhorskiy, J. W. Manweiler, H. E. Spence, H. J. Singer, S. G. Claudepierre, B. A. Larsen, A. R. Soto-Chavez, and R. J. Cohen (2017), Second harmonic poloidal waves observed by Van Allen Probes in the dusk-midnight sector, *J. Geophys. Res. Space Physics*, *122*, 3013–3039, doi:10.1002/2016JA023770.

Received 2 DEC 2016
Accepted 17 FEB 2017
Accepted article online 24 FEB 2017
Published online 7 MAR 2017

Abstract This paper presents observations of ultralow-frequency (ULF) waves from Van Allen Probes. The event that generated the ULF waves occurred 2 days after a minor geomagnetic storm during a geomagnetically quiet time. Narrowband pulsations with a frequency of about 7 mHz with moderate amplitudes were registered in the premidnight sector when Probe A was passing through an enhanced density region near geosynchronous orbit. Probe B, which passed through the region earlier, did not detect the narrowband pulsations but only broadband noise. Despite the single-spacecraft measurements, we were able to determine various wave properties. We find that (1) the observed waves are a second harmonic poloidal mode propagating westward with an azimuthal wave number estimated to be ~100; (2) the magnetic field fluctuations have a finite compressional component due to small but finite plasma beta (~0.1); (3) the energetic proton fluxes in the energy ranging from above 10 keV to about 100 keV exhibit pulsations with the same frequency as the poloidal mode and energy-dependent phase delays relative to the azimuthal component of the electric field, providing evidence for drift-bounce resonance; and (4) the second harmonic poloidal mode may have been excited via the drift-bounce resonance mechanism with free energy fed by the inward radial gradient of ~80 keV protons. We show that the wave active region is where the plume overlaps the outer edge of ring current and suggest that this region can have a wide longitudinal extent near geosynchronous orbit.

1. Introduction

Electromagnetic pulsations in the Pc4–5 band (period range = 45–600 s) are commonly observed in the terrestrial magnetosphere and are typically poloidal mode hydromagnetic waves standing on a closed geomagnetic field line [*Cummings et al.*, 1969; *Kivelson and Southwood*, 1985; *Walker*, 1987]. Consequently, these waves are remarkably monochromatic. The poloidal mode indicates that the magnetic field and bulk flow velocity fluctuations (b_v and V_v, respectively) are radially polarized (more precisely along the field line curvature), while the electric field fluctuations (E_ϕ) are azimuthally polarized. Previous studies reported that frequencies of these waves correspond to either the fundamental or second harmonic eigenfrequencies of the corresponding field lines [e.g., *Singer et al.*, 1982; *Takahashi et al.*, 1990; *Claudepierre et al.*, 2013; *Dai et al.*, 2013; *Korotova et al.*, 2015]. The poloidal waves with the fundamental frequency are often detected as giant pulsations on the ground [*Takahashi and Anderson*, 1992; *Takahashi et al.*, 1992; *Glassmeier et al.*, 1999; *Takahashi et al.*, 2011], while the poloidal waves with the second harmonic frequency are most frequently observed in the terrestrial magnetosphere [*Hughes et al.*, 1978a; *Singer et al.*, 1982; *Takahashi et al.*, 1990; *Dai et al.*, 2015]. In ideal cases [e.g., *Cummings et al.*, 1969] (that is, conditions with sufficiently small beta $\beta = 8\pi nT/B^2$ and infinite azimuthal wave number *m*), the transverse electric and magnetic field components are in quadrature (±90° phase difference with the sign depending on the harmonic number and magnetic latitude of observation). Therefore, in principle the phase relationship among E_ϕ, b_v, and V_v can be used to distinguish between the first and second harmonic poloidal waves [e.g., *Motoba et al.*, 2015]. In the real magnetosphere, poloidal waves are coupled with toroidal and compressional waves [e.g., *Kivelson and Southwood*, 1986; *Walker*, 1987;

Chen and Hasegawa, 1988, 1991], and hence observations show poloidal waves usually accompanying finite compressional and toroidal components [e.g., *Hughes et al.*, 1979; *Dai et al.*, 2015].

The poloidal mode waves usually have a large m number of the order of tens to hundreds, which means that instabilities responsible for the wave excitation should be capable of generating waves with a short azimuthal wavelength. These waves are most likely generated by instabilities within the magnetosphere associated with the ring current population (internal source). Observationally, two types of internally driven (i.e., with a large m number) ULF waves are most frequently observed: one is a compressional Alfvén type wave, which has a dominant compressional magnetic field component, and the other is a transverse Alfvén type wave, which has a dominant transverse component [e.g., *Cheng and Qian*, 1994; *Dai et al.*, 2015]. The former is often associated with large β, anisotropic pressure plasmas observed during the main phase of geomagnetic storms, whereas the latter tends to occur in the late recovery phase of geomagnetic storms. Linear theory suggests that β of energetic particles is an important parameter that determines the instability likely operating [*Southwood*, 1976; *Chen and Hasegawa*, 1988, 1991; *Dettrick et al.*, 2003]. In the small β regime ($\beta \lesssim 0.1$), the transverse Alfvén mode can be destabilized via drift-bounce wave-particle interactions. The most unstable mode tends to have a second harmonic standing wave structure and a wavelength comparable to the gyroradius ρ_L of energetic particles in resonance ($k_\perp \rho_L \sim 0.5$) [*Chen and Hasegawa*, 1988; *Dettrick et al.*, 2003]. The latter readily indicates that the waves should have a large m number because the gyroradius of ring current ions is usually much smaller than the typical magnetospheric length scale. In the large β regime ($\beta \gg 1$), the ballooning mode is coupled to the compressional mode, such as the drift mirror mode [*Hasegawa*, 1969], whose free energy source is the pressure anisotropy, or the drift-compressional mode [*Crabtree and Chen*, 2004], whose free energy source is the pressure inhomogeneity. In the intermediate β regime ($\beta \sim 1$), the finite coupling between the compressional and transverse modes becomes important. In this situation, the more general drift Alfvén ballooning mirror instability becomes most unstable and has the properties intermediate of the waves generated in the small and large β regimes [*Chen and Hasegawa*, 1991].

Fundamental mode poloidal waves are known to play an important role in the transport of radiation belt electrons. Drift resonant interactions between small m poloidal (and toroidal) waves and relativistic electrons drifting in an asymmetric magnetic field were quantified by *Elkington et al.* [1999, 2003]. Because amplitudes of the externally driven, small m mode ULF waves rapidly decrease with decreasing L [*Vassiliadis et al.*, 2007; *Rae et al.*, 2012], radial transport by the small m number ULF waves is most effective at large L shells. On the other hand, the large m number poloidal waves excited via internal sources were thought to be less important to overall radiation belt dynamics because the relativistic electrons can only interact with the high-frequency pulsations, and wave power in the ULF spectrum is typically a decreasing function of frequency [e.g., *Elkington*, 2006]. However, *Ukhorskiy et al.* [2009] showed that the large m number poloidal waves can also cause localized random scattering of equatorial electrons, which can be described by a diffusive process. Because the wavelength is substantially smaller than the electron drift orbit scale, these large m number waves can cause local violation of the third invariant of trapped electrons. Consequently, the internally driven large m number waves can radially transport relativistic electrons inside geosynchronous orbit where the global, small m number waves are less effective. *Georgiou et al.* [2015] showed that the earthward penetration of Pc5 waves, which are a consequence of the combined effects of external and internal sources, are indeed associated with outer radiation belt electron enhancements.

Of particular interest in the present study is a class of radially polarized second harmonic transverse pulsations occurring outside of the plasmapause [*Takahashi and Anderson*, 1992]. *Engebretson et al.* [1992] studied several wave events of this class observed in the noon and dusk sectors and found that (1) these pulsations occur in a longitudinal extent ranging from 1.5 to 8 h in magnetic local time and a narrow extent in L shell and are found in regions far outside the plasmasphere but of density characteristic of the outer plasmasphere ($n_e \sim 10\ \mathrm{cm}^{-3}$); (2) the associated geomagnetic conditions are quiet, usually after geomagnetic storms; (3) plasma beta associated with the pulsations ranges roughly from 0.1 to 1; and (4) wave onset often occurs within 1 h after sharp drops in the *AE* index to values of 100 or below. Based on the observational clues, *Engebretson et al.* [1992] concluded that these pulsations can be excited by an instability source that covers some longitudinal extent, but the local plasma density plays an important role in controlling the wave onset by altering local field line resonance conditions. The controlling effect of the local plasma density was also observationally shown [*Liu et al.*, 2013; *Dai et al.*, 2015]. *Engebretson et al.* [1992] further suggested based on theoretical work that waves can still be excited during quiet geomagnetic activity because after several days from ring current injections the low-energy (~1 keV) ring current population, which contributes to

stabilization of the waves, decays away while high-energy (~100 keV) population remains sufficiently dense to drive the drift-bounce resonance instability. *Vetoulis and Chen* [1994, 1996] provided theoretical explanation for the radial localization of the poloidal waves. They suggested that the poloidal waves can be radially bound by the sufficiently strong, radially inward pressure gradient (the outer edge of the ring current), creating a dip in the poloidal Alfvén frequency with respect to *L*. This pressure gradient creates a "potential well" localized in *L* within which the second harmonic poloidal mode is most likely trapped. *Denton et al.* [2003] tested this theory and found that such a dip in the poloidal frequency is associated with the radial localization but may instead result from the background density or magnetic field. Previous theoretical studies [e.g., *Southwood*, 1976; *Chen and Hasegawa*, 1988, 1991] indeed suggest that the second harmonic poloidal mode is most unstable and for adiabatic distributions free energy can be fed by the radial gradient at the outer edge of ring current. However, the proposed wave excitation mechanism has yet to be observationally confirmed.

In the present study, we present Van Allen Probes observations of poloidal waves of this class. We analyze wave and particle data to determine the wave properties and interpret the energetic particle flux pulsations. We then examine the free energy source and the wave generation mechanism based on observational data. Finally, we use the measured plasma conditions and the separate poloidal mode wave measurements from the geosynchronous satellites to deduce a global picture of the wave active region. The results are compared with the theoretical predictions by *Chen and Hasegawa* [1988, 1991] and the statistical results of *Engebretson et al.* [1992]. The present paper is organized as follows. Section 2 describes experiments and data set, section 3 presents field and particle observations, and section 4 analyzes them in detail to determine various wave properties. Section 5 discusses radial and longitudinal extents of wave activity, and section 6 concludes the study.

2. Experiments and Data

The primary data used in the present study are provided by the Van Allen Probes (also known as Radiation Belt Storm Probes or RBSPs). The twin spacecraft, which were identically instrumented, were launched into an orbital configuration of $1.1 \times 5.8\, R_E$ equipped with a suite of state-of-the-art particle and wave experiments [*Mauk et al.*, 2013]. The spacecraft are spin stabilized with a spin period of ~11 s, and the spin axis is maintained within 27° of the Sun-Earth line. In addition to RBSP data, the magnetometer and energetic proton measurements from the space environment monitor [*Grubb et al.*, 1996; *Heckman et al.*, 1996] on board the Geostationary Environmental Satellite System (GOES) spacecraft are also used to examine wave activity at geosynchronous orbit.

The Electric and Magnetic Field Instrument and Integrated Science (EMFISIS) instrumentation suite provides measurements of DC magnetic fields with a 64 vectors/s sampling cadence [*Kletzing et al.*, 2013]. It also provides high-frequency (from 10 to 400 kHz) electric field measurements, allowing an accurate determination of the electron density obtained from the upper hybrid resonance frequency line [*Kurth et al.*, 2015; *Zhelavskaya et al.*, 2016]. Electric fields are provided by the Electric Fields and Waves (EFW) experiment that consists of two pairs of spherical double-probe sensors in the spin plane and a third pair along the spin axis [*Wygant et al.*, 2013].

Low- and medium-energy ions are provided by the Energetic Particle, Composition, and Thermal Plasma (ECT) suite [*Spence et al.*, 2013]. The Helium, Oxygen, Proton, and Electron (HOPE) Mass Spectrometer measures low-energy ion species (H^+, He^+, and O^+) in the energy range from ~1 eV to ~50 keV [*Funsten et al.*, 2013]. The Magnetic Electron Ion Spectrometer (MagEIS) uses a two-parameter magnetic focusing technique to measure electrons from 20 to 4000 keV and protons from 60 to 1000 keV [*Blake et al.*, 2013].

The Radiation Belt Storm Probes Ion Composition Experiment (RBSPICE) is a time-of-flight versus total energy instrument that measures ions (mainly H^+, He^+, and O^+) over the energy range from ~20 keV to ~1 MeV [*Mitchell et al.*, 2013]. Ion energy measurements are combined with coincident time-of-flight measurements to derive particle mass and identify particle species. Like the HOPE experiment, the RBSPICE experiment measures near-full 3-D distributions of ions with six solid-state telescopes arranged in 160° meridional plane (no observation near the Sun direction). This paper uses proton fluxes from this experiment for detailed analysis. The proton fluxes are provided with two data products, one covering between about 10 keV and about 50 keV (called ToFxPH) and another covering above 50 keV (called ToFxE).

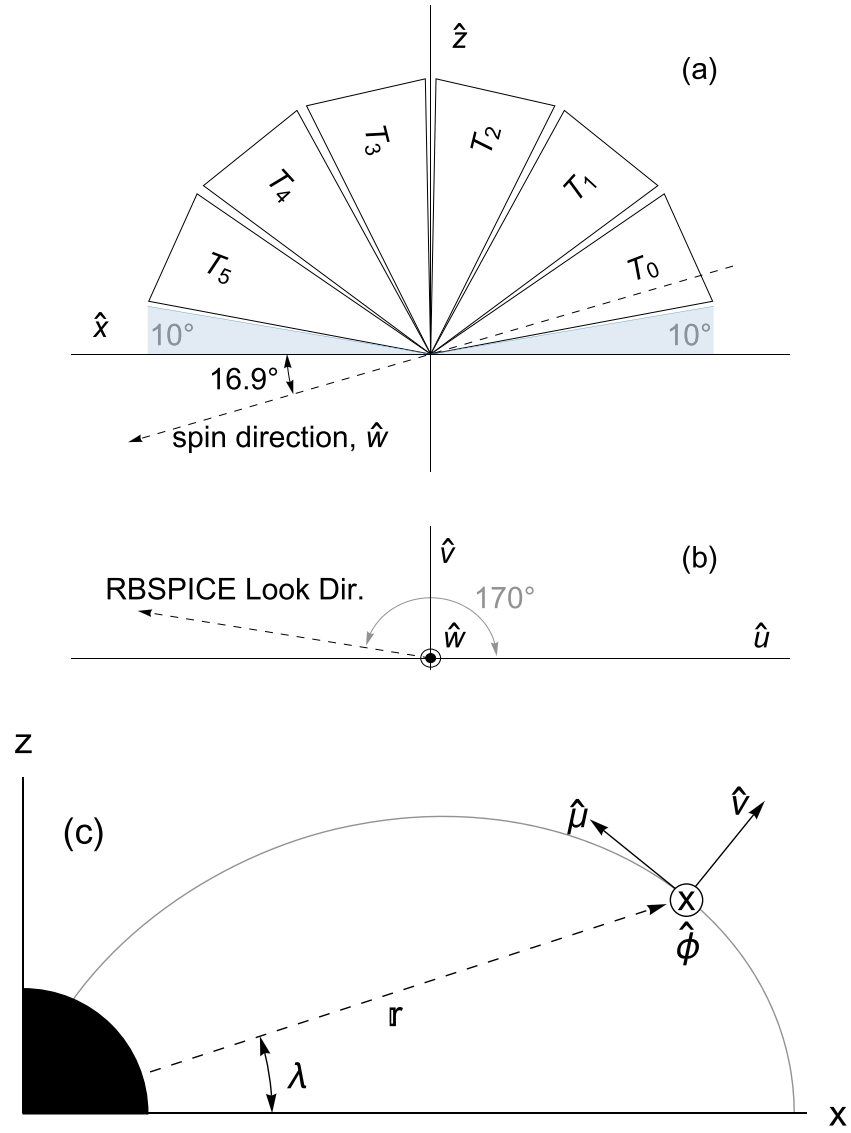

Figure 1. (a and b) RBSPICE mounting position in the science (UVW) coordinate system. Six solid-state telescopes are labeled T_j with $j = 0, 1, \cdots, 5$. (c) The mean-field-aligned coordinate system.

Figure 1c displays the coordinate system used throughout the paper. It is a local magnetic mean-field-aligned (MFA) coordinate system where $\hat{\mu}$ is parallel to the background magnetic field **B**, $\hat{\phi}$ is parallel to $\mathbf{B} \times \mathbf{r}$, and $\hat{v}$ completes the right-handed orthogonal system. Here **r** is the position vector from Earth's center to a point on the field line, and **B** is the background magnetic field, which is defined to be a 20 min running average of the measured magnetic field. Symbols with subscript "0" (e.g., B_0 and r_0) represent quantities on the magnetic equator mapped along the field line. The L shell is defined so that $r_0 = LR_E$ where R_E is the Earth's radius. The perturbed electric and magnetic field vectors will be denoted by **E** and **b**, respectively.

3. Observations

Figure 2 shows the solar wind condition and geomagnetic indices. A minor geomagnetic storm with a minimum *Dst* value of about −60 nT occurred right after 18 May 2013, perhaps triggered by the sudden increase of the solar wind dynamic pressure and the southward component of the interplanetary magnetic field. Over the course of 2 days, the solar wind parameters returned to a normal condition, and ring current gradually decayed. On 20 May 2013, the solar wind dynamic pressure suddenly increased, but the *Dst* index remained relatively unchanged. The *AE* index exhibited three large enhancements (with maxima at about 1000 nT)

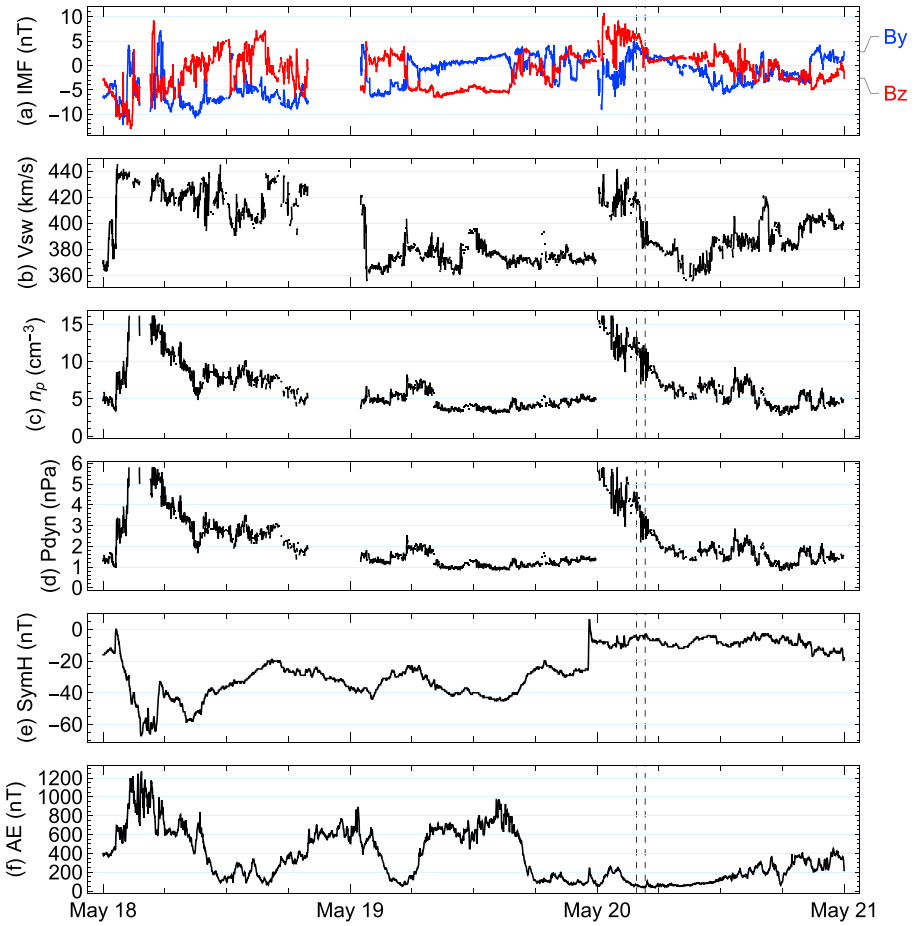

Figure 2. Time series of solar wind parameters and geomagnetic indices. (a) Interplanetary magnetic field (IMF) B_y and B_z in the geocentric solar magnetospheric (GSM) coordinate system, (b) solar wind speed, (c) solar wind proton density, (d) solar wind dynamic pressure, (e) *SYM-H* index, and (f) *AE* index. The vertical dashed lines mark the period of interest between 0350 UT and 0440 UT on 20 May 2013.

during the storm main and recovery phases and remained relatively small (~100 nT) after 1800 UT on 19 May 2013 until 1200 UT the next day. The two vertical dashed lines between 0350 and 0440 UT mark the period when RBSP-A detected the ULF pulsations and energetic proton flux pulsations (during the outbound pass); this period will be referred to as period of interest. The event occurred roughly 4 h after the second dynamic pressure pulse and roughly 10 h after the *AE* index dropped down to a value of 200 nT or below.

Figure 3 shows orbital plots of RBSP-A, RBSP-B, and GOES-15. The thick curves represent the orbital segments during the period of interest. RBSP-B was leading RBSP-A by about 2 h (in UT), and the apogees of both spacecraft were located at about 17° magnetic latitude and about 2200 h in magnetic local time. The GOES-15 spacecraft stayed close to the magnetic equator throughout and was separated from RBSP-A by about 2.6 h in magnetic local time when RBSP-A detected the wave event.

Figure 4 shows power spectral densities of the electric and magnetic fields from RBSP-A in the MFA coordinate system. For the electric field, the spin component of the electric field was determined using the $\mathbf{E} \cdot \mathbf{B} = 0$ condition so the parallel component of the electric field fluctuations is assumed to be 0. During the period shown in the figure, the magnitude of the spin component of the magnetic field was sufficiently large such that the angle between the spin axis and the magnetic field vector was about 56° near the apogee. Therefore, the error in estimating the spin component of the electric field caused by division is expected to be small.

Figure 4 suggests that all components of the electric and magnetic fields exhibit at least two narrow bands in frequency space: one at about 7 mHz and another at around 12 mHz. The band near 7 mHz is most pronounced and persists between 0350 and 0630 UT (with a power reduction near 0510 UT), whereas the band near

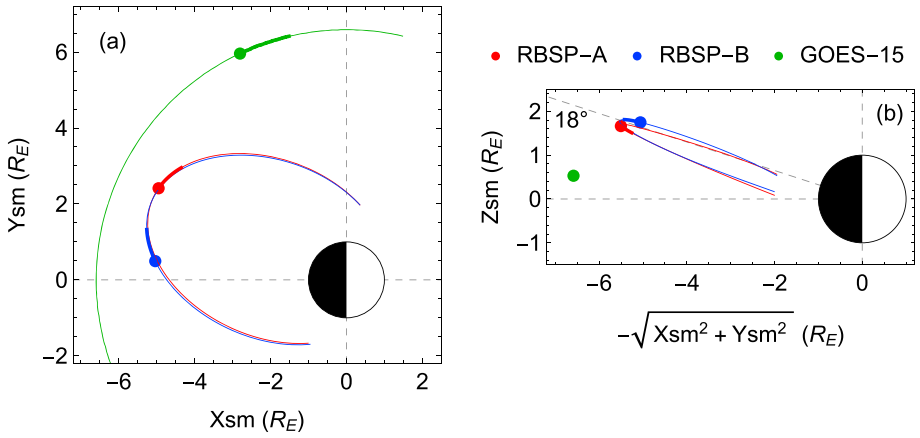

Figure 3. (a) Equatorial and (b) meridional projections of the RBSP-A, RBSP-B, and GOES-15 spacecraft orbits in the Solar Magnetospheric (SM) coordinates. Thick curves represent the orbital segments of the spacecraft from 0350 UT to 0440 UT. The spacecraft are heading toward the solid dots.

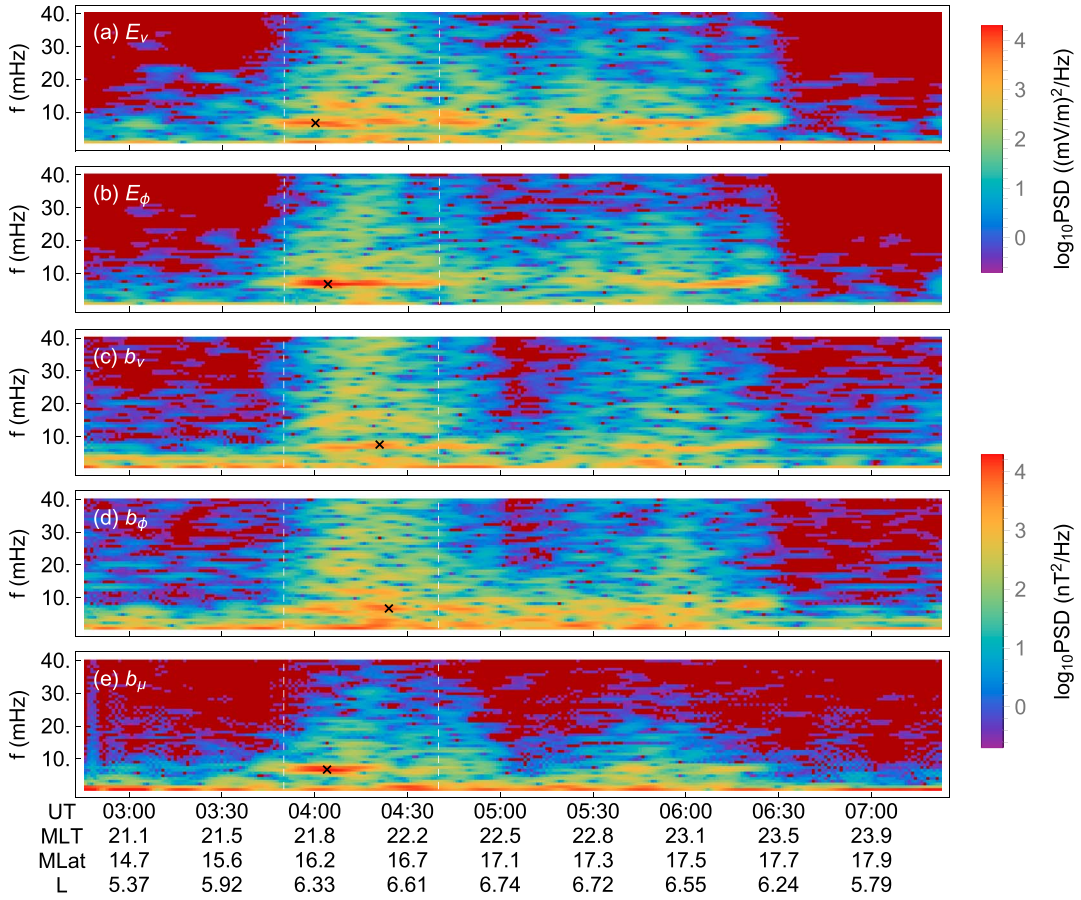

Figure 4. Power spectral density of the electric and magnetic fields measured by RBSP-A. (a and b) Power spectral density of the two perpendicular components of the electric field in the MFA coordinate system. (c–e) Power spectral density of the three components of the magnetic field in the MFA coordinate system. The dark red region is where the spectral power is below the lower limit of color scales. The vertical dashed lines mark the period of interest. The cross symbols locate where maximum value of each component occurs (above 4 mHz). The maximum values for E_v and E_ϕ power are about 10^4 and 2.5×10^4 (mV/m)^2/Hz, respectively. The maximum values for b_v, b_ϕ, and b_μ power are about 0.5×10^4, 0.7×10^4, and 2.2×10^4 nT^2/Hz, respectively.

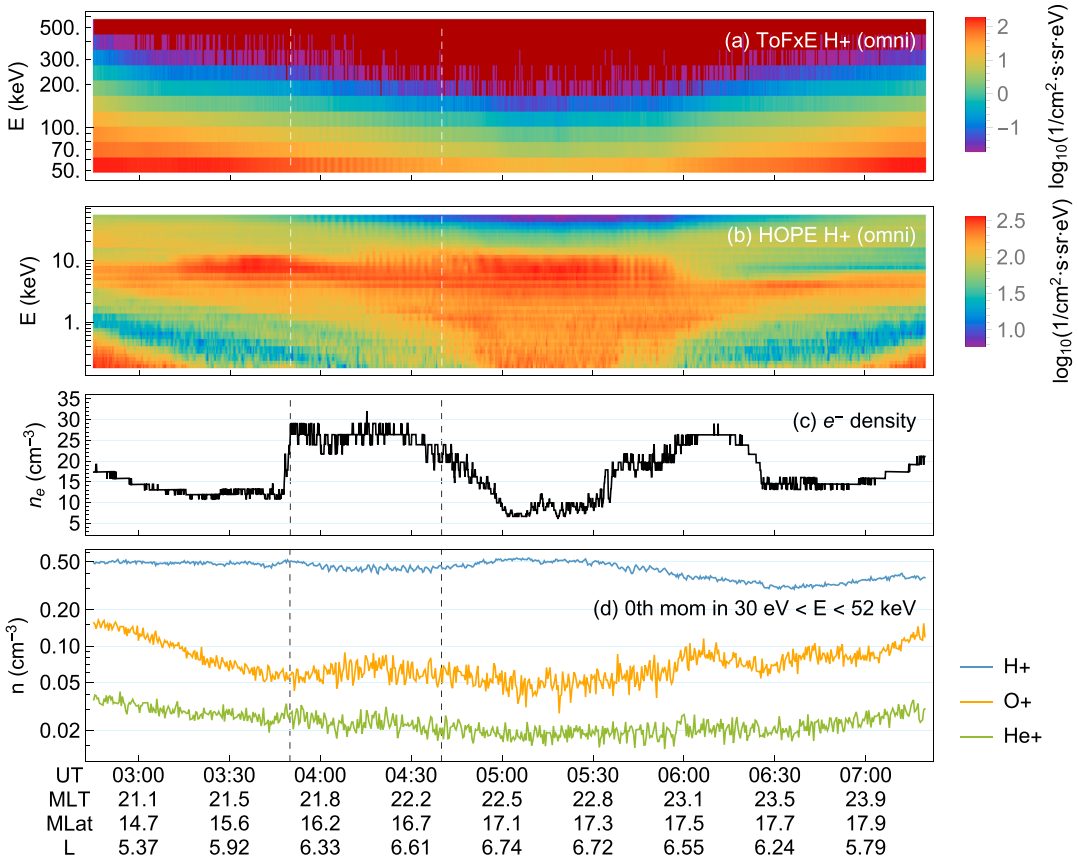

Figure 5. RBSP-A measurements of (a) omnidirectional differential proton fluxes from RBSPICE (ToFxE), (b) omnidirectional differential proton fluxes from HOPE, (c) total electron density estimated from upper hybrid frequencies, and (d) number densities of three major ion species measured by HOPE (30 eV and above). The vertical dashed lines mark the period of interest.

12 mHz (and, if any, higher harmonics) is very faint. Focusing on the 7 mHz band during the period of interest, one can see that the poloidal component of the electric field (E_ϕ) has larger wave power than the toroidal component (E_v), indicating that the associated waves can be classified as a poloidal mode. (The ratio of maximum power of E_ϕ to E_v is about 2.5.) In contrast, the magnetic field fluctuations have a relatively strong compressional component (b_μ) but rather weak poloidal (b_v) and toroidal (b_ϕ) components. (The maximum power of b_μ is roughly 4 times larger than that of the other components.)

Figure 5 shows the corresponding particle measurements. The total electron density n_e estimated from the upper hybrid frequency line suggests that RBSP-A passed through an enhanced density region that is narrow in the radial direction (about 0.5 R_E). In addition, because the densities of the three major ion species of energy above 30 eV are relatively unchanged (Figure 5d), the total density increase is dominantly contributed by the cold population whose origin may be a residual plume [*Goldstein et al.*, 2014a, 2014b]. Comparing n_e with the wave power spectrum in Figure 4, it is apparent that wave activity is confined within the two enhanced density regions. Particularly, the stronger wave activity occurred during the first pass of the increased density region. Associated with the wave activity, energetic proton fluxes also exhibit fluctuations manifested by the fine vertical stripes in the energy range from about 1 keV to about 100 keV, which is discussed in the next paragraph.

Figure 6a shows fluctuations of the electric and magnetic field components during the period of interest. All three components of the magnetic field contain high-frequency oscillations (especially evident in b_μ) because the spacecraft spin effect has not been removed completely. Due to the narrowband nature as shown in Figure 4, the fluctuations of E_ϕ, E_v, and b_μ are very monochromatic. In contrast, fluctuations of b_v and b_ϕ are

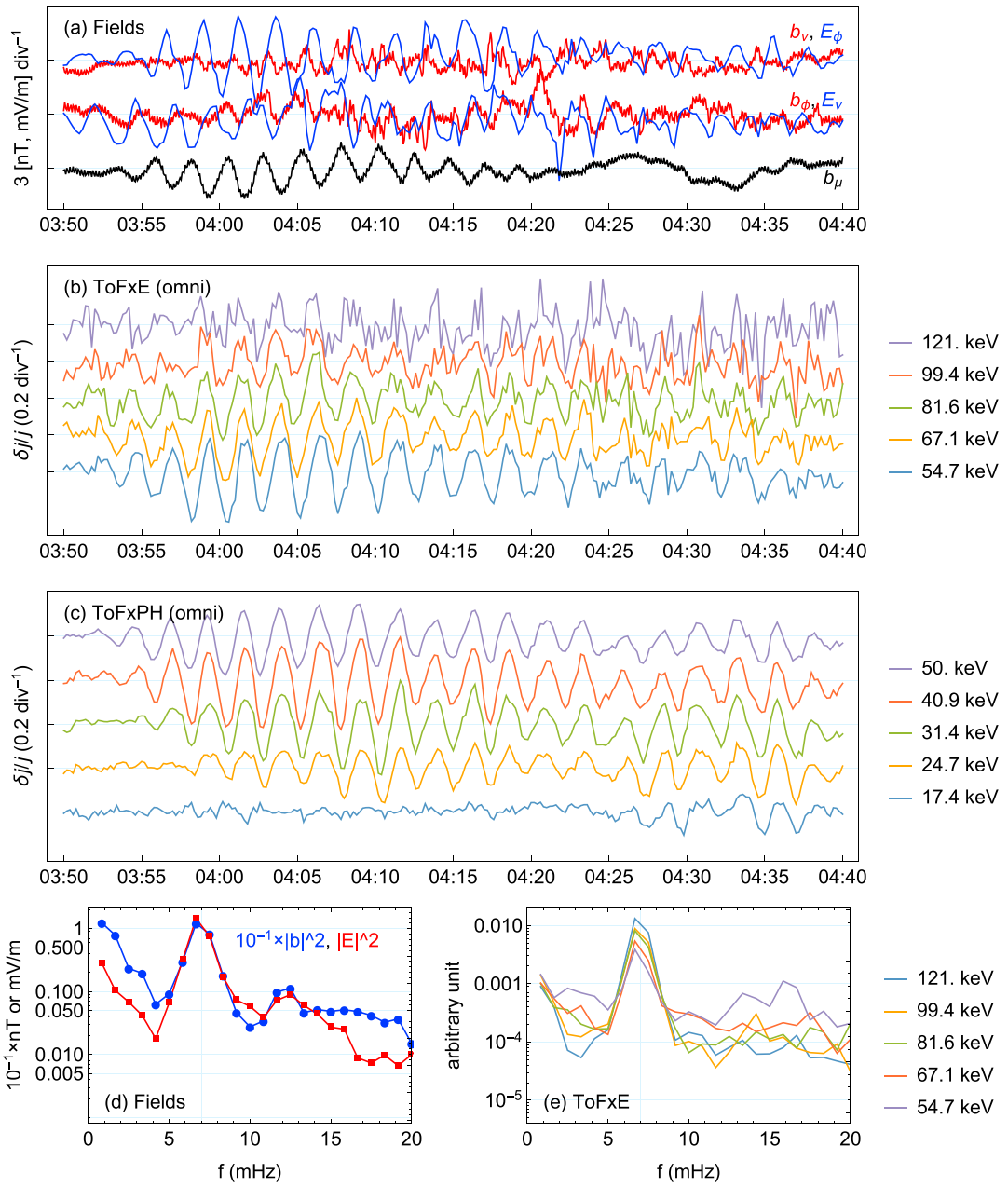

Figure 6. (a–c) Pulsations of the electric and magnetic field components and energetic proton residual fluxes (from RBSPICE) between 0350 and 0440 UT. For the magnetic field and residual flux pulsations, a 20 min running average has been subtracted. (d and e) Power spectral densities of the fields and residual fluxes (>50 keV protons).

less monochromatic and have weaker amplitudes. Figures 6b and 6c show the omnidirectional proton residual fluxes measured by the RBSPICE experiment. Similar to previous studies [*Takahashi et al.*, 1990; *Motoba et al.*, 2015], the residual fluxes are defined by $\delta \log j \sim (j - j_{\mathrm{back}})/j_{\mathrm{back}}$, where a 20 min running average of j is taken to be the background flux j_{back}. The fluctuations of the residual fluxes in all but the 17.4 and 121 keV channels are also monochromatic. Figure 6d shows electric and magnetic field power spectral densities calculated from the field fluctuations in Figure 6a. Likewise, Figure 6e shows residual flux power spectral densities calculated from the residual fluxes in Figure 6b. A pronounced peak is located at about 7 mHz for both the electric and magnetic fields and the residual fluxes. In addition, the electric and magnetic field power has a distinct secondary peak near 12 mHz, which is also shown in Figure 4 and which may be a higher harmonic mode.

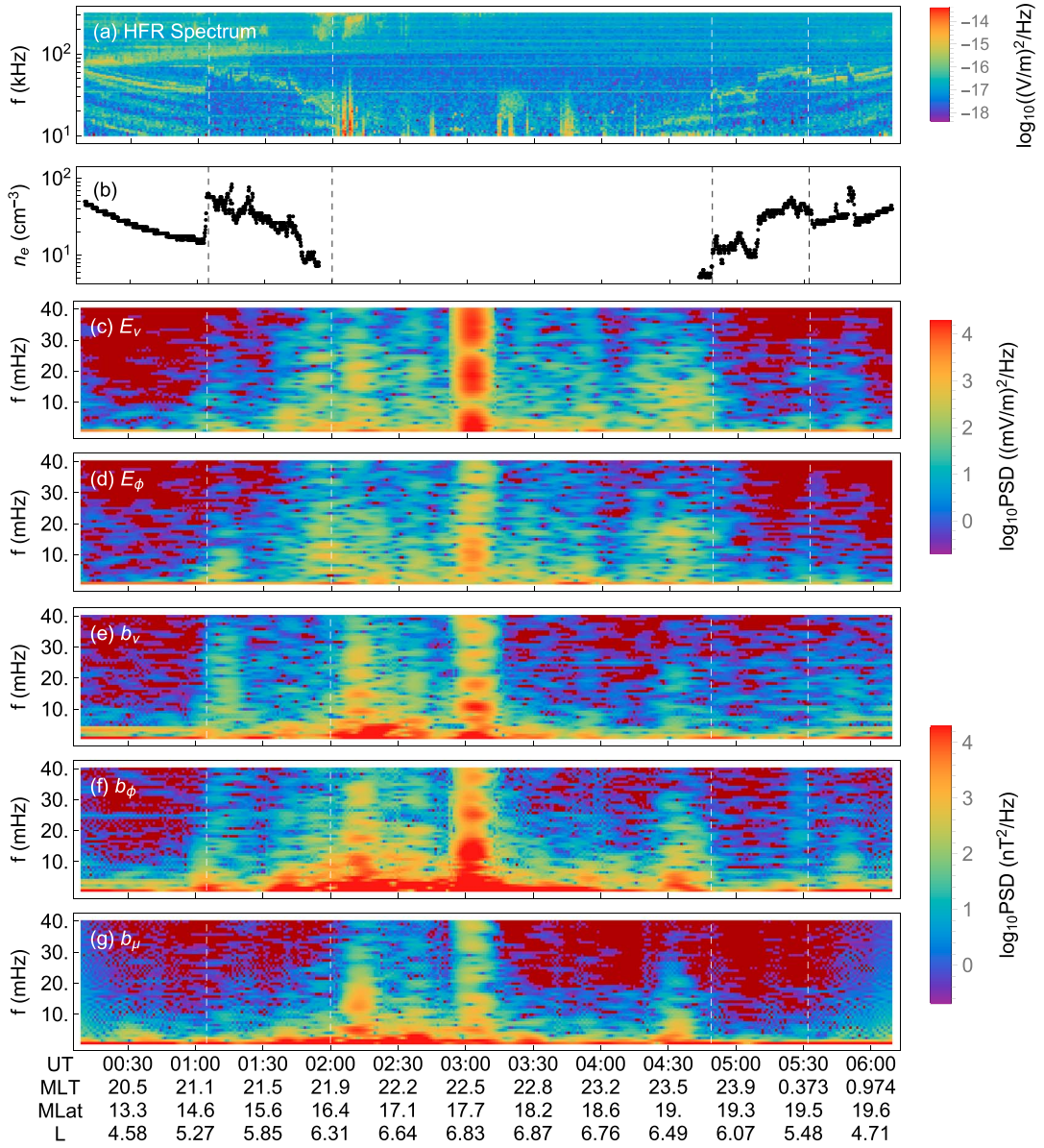

Figure 7. (a) High-frequency electric field power spectrum. (b) Total electron density derived from the upper hybrid frequency line. (c–g) Power spectral density of the electric and magnetic fields measured by RBSP-B with the format the same as that of Figure 4.

Figure 7 shows electric and magnetic field power spectral densities from RBSP-B. Based on the upper hybrid frequency line and the total electron density derived from it (Figures 7a and 7b), RBSP-B also passed through the enhanced density region between 0100 and 0200 UT (first two vertical dashed lines) and between 0450 and 0530 UT (last two vertical dashed lines). Although it has an orbit similar to that of RBSP-A, RBSP-B observed mostly broadband noise, even within the elevated density regions. We also analyzed the energetic proton measurements from RBSP-B but did not find any particular signature of wave modulation or resonance (not shown). One possible explanation is that the waves were more broadbanded or not present when RBSP-B passed through the wave region and then they were coupled to a standing wave when RBSP-A went through the same region. Another possibility is the slightly different orbital configuration between the two spacecraft. As shown in Figure 3b, the orbit of RBSP-B is slightly more inclined than that of RBSP-A. Consequently, RBSP-B was mapped to the equatorial region farther out than RBSP-A and could have swept through the wave region more quickly without registering the wave activity.

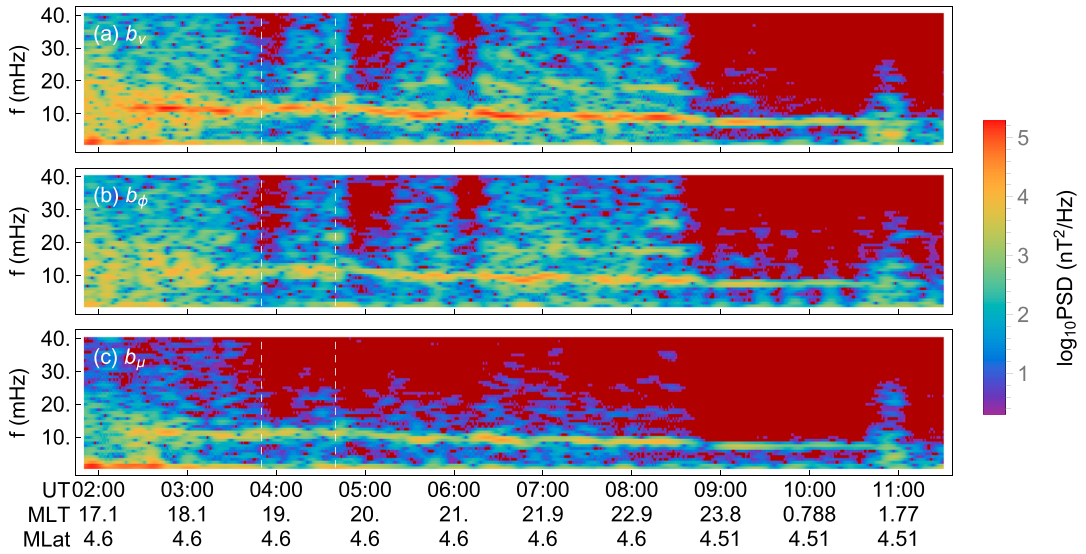

Figure 8. Power spectral density of the magnetic field measured by GOES-15. The format is the same as that of Figure 4.

Another interesting observation comes from the GOES-15 spacecraft. Figure 8 shows power spectral densities of the magnetic field. It clearly shows that there was narrowband wave activity persistent for about 9 h. The frequency of the waves was about 12 mHz near the dusk sector (beginning of the plot), gradually decreased, and reached about 8 mHz right after the midnight meridian. This gradual frequency variation is a typical feature related to the plasma density varying with local time [*Takahashi and Denton*, 2007]. Large amplitudes of the b_v component compared to the other two components and the proximity of the spacecraft to the magnetic equator (within 5° magnetic latitude) indicate that the observed waves are an even harmonic poloidal mode standing wave [e.g., *Motoba et al.*, 2015]. During the period of interest (vertical dashed lines), RBSP-A and GOES-15 were separated by about 2.6 h in magnetic local time.

4. Detailed Analyses

In this section, we investigate the wave properties (that is, the *m* number and the nodal structure of the poloidal waves) and interpret energetic proton fluctuations observed simultaneously with the waves. The analysis is based on the wave and particle observations made by RBSP-A during the outbound pass through the enhanced density region.

4.1. Azimuthal Wave Number

Propagation of a wave signal can be determined by using a pairing of field measurements from multiple satellites [e.g., *Hughes et al.*, 1978b; *Takahashi et al.*, 2013] or by using finite Larmor radius effects of energetic particles observed at a single spacecraft [*Su et al.*, 1977; *Kivelson and Southwood*, 1983; *Lin et al.*, 1988]. The wavelength to be measured must be longer than the satellite separation or the gyroradius of the particles, respectively.

Kivelson and Southwood [1983] described that the spacecraft spin phase dependence can occur in the particle distributions when $\rho_L \sim \lambda_\perp$, where ρ_L is the gyroradius of a particle and $\lambda_\perp$ is the wavelength associated with the wave number perpendicular to **B**. Imagine that a single particle detector is oriented perpendicular to the spin axis, which is in turn parallel to **B**. At a given time and look direction, the detector detects particles whose gyrocenters are located away from the spacecraft by ρ_L. As the spacecraft completes one spin, the detector measures particles whose gyrocenters are located at different phases of a wave [see *Kivelson and Southwood*, 1983, Figure 6]. Therefore, spin modulation is expected in measured particle distributions. Assuming that the particle flux at the gyrocenter varies with $\exp(i\mathbf{k}_\perp \cdot \mathbf{r} - i\omega t)$ at a position **r** due to interactions with the electric field perturbations, the spin modulation of the flux *j* seen by the spacecraft may be expressed as $j \sim \exp(i\mathbf{k}_\perp \cdot \vec{\rho}_L - i\omega t)$ [*Su et al.*, 1977; *Kivelson and Southwood*, 1983]. Here $\mathbf{k}_\perp$ is the perpendicular wave number, ω is the wave frequency, and $\vec{\rho}_L$ is the gyroradius times the gyrocenter direction. The gyrocenter direction is periodic in time with a period equal to the spacecraft spin period [see *Kivelson and Southwood*, 1983, Figure 6]. Apparently, the spin period should be less than the wave period to observe the spin modulation.

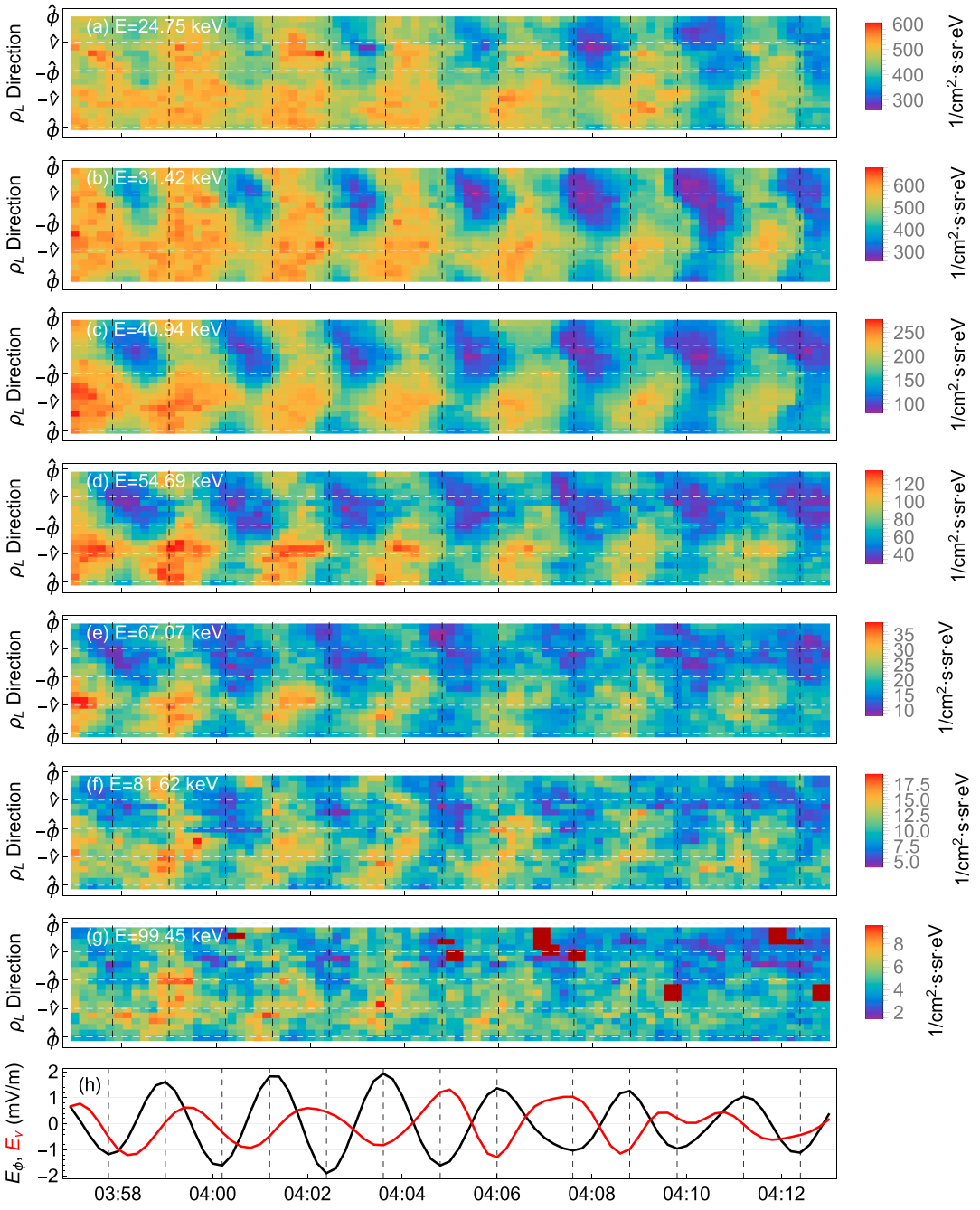

Figure 9. (a–g) Local 90° pitch angle proton fluxes obtained from the RBSPICE experiment organized in the gyrocenter direction and time. (h) Azimuthal (black) and radial (red) components of the electric field oscillations from Figure 6a (these have been bandpass filtered between 3 and 11 mHz). The vertical dashed lines mark local minima and maxima of E_ϕ.

In practice, the spin axis of a satellite is not aligned with **B**, nor is **B** static. Due mainly to the alignment of the spacecraft, estimates of *Su et al.* [1977] had large uncertainties. However, satellites can carry more than one detector. The multiple detectors simultaneously scan the polar angle relative to the spin axis and after one full spin provide particle measurements in a 4π direction. This allowed *Lin et al.* [1988] to unambiguously determine wave propagation by examining 90° pitch angle ion fluxes from back-to-back detectors although the spin axis of the spacecraft was not aligned with **B**.

In this study, because only RBSP-A registered the poloidal waves, we examine spin modulation of energetic proton fluxes obtained from the RBSPICE experiment to determine the *m* number. As shown in Figures 1a

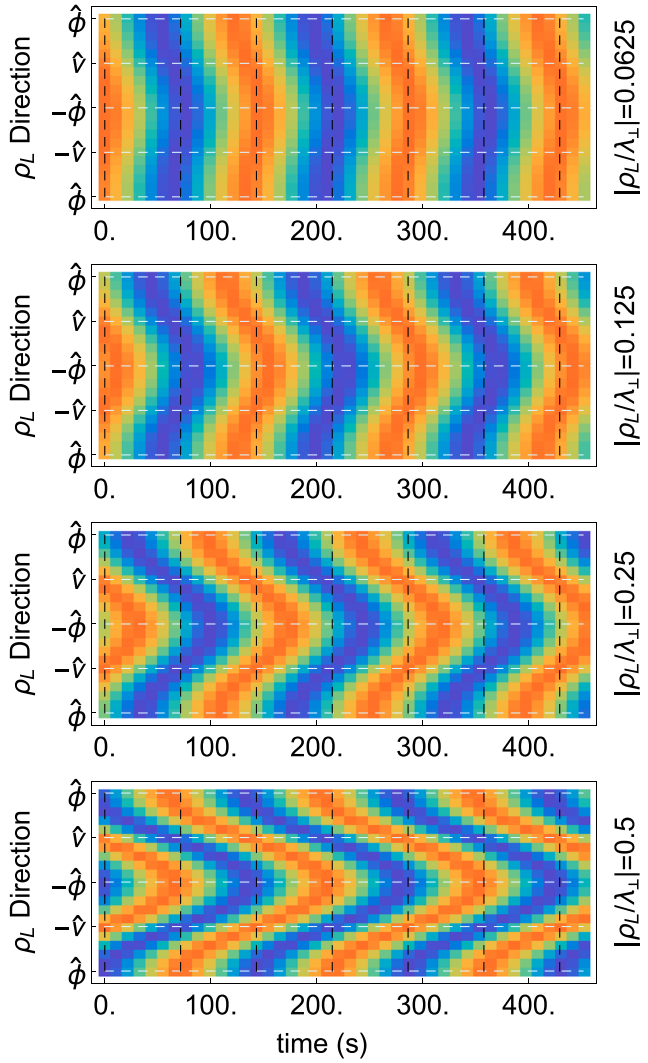

Figure 10. Modeled spin modulation using equation (1) for $\rho_L/\lambda_\perp = \frac{1}{16}, \frac{1}{8}, \frac{1}{4}$, and $\frac{1}{2}$.

and 1b, RBSPICE is mounted on a 16.9° bracket on the bottom spacecraft deck and 170° away from the *U* direction (the science coordinate system is called UVW coordinate system) [*Mitchell et al.*, 2013]. Here *W* direction is along the spacecraft spin direction. Because the magnetic field data are provided in both the UVW coordinate system (level 2 data set) and the Geocentric Solar Ecliptic (GSE) coordinate system (level 3 data set), and the spacecraft spin direction in the GSE coordinate system is included in the EFW spinfit data set, one can construct a coordinate transform that translates the RBSPICE look direction into the gyrocenter direction. For a more accurate estimate, we focus on the period between 0357 and 0413 UT during which E_ϕ and 10s of keV protons are well correlated.

In Figure 9, the local 90° pitch angle proton fluxes from the seven energy channels are plotted as a function of gyrocenter direction and time. In addition to the long-period fluctuations with the same frequency as E_ϕ and E_v (Figure 9h), the fluxes also exhibit shorter-period spin (or gyrocenter direction) modulation. The phase difference between E_ϕ and E_v changes with time, but it is roughly 180° between 0402 and 0410 UT. Based on visual inspection, the long-period fluctuations of the proton fluxes appear to be correlated with E_ϕ better than with E_v. In all energy channels, the flux modulation at the $\hat{\phi}$ direction leads the flux modulation at the opposite direction, while the modulations at the $\hat{v}$ and $-\hat{v}$ directions are roughly in phase. This phase relationship indicates that the wave is propagating in the $-\hat{\phi}$ direction (westward) because protons whose gyrocenters are located eastward of the spacecraft are affected by the waves first. A noteworthy feature is that the flux at the

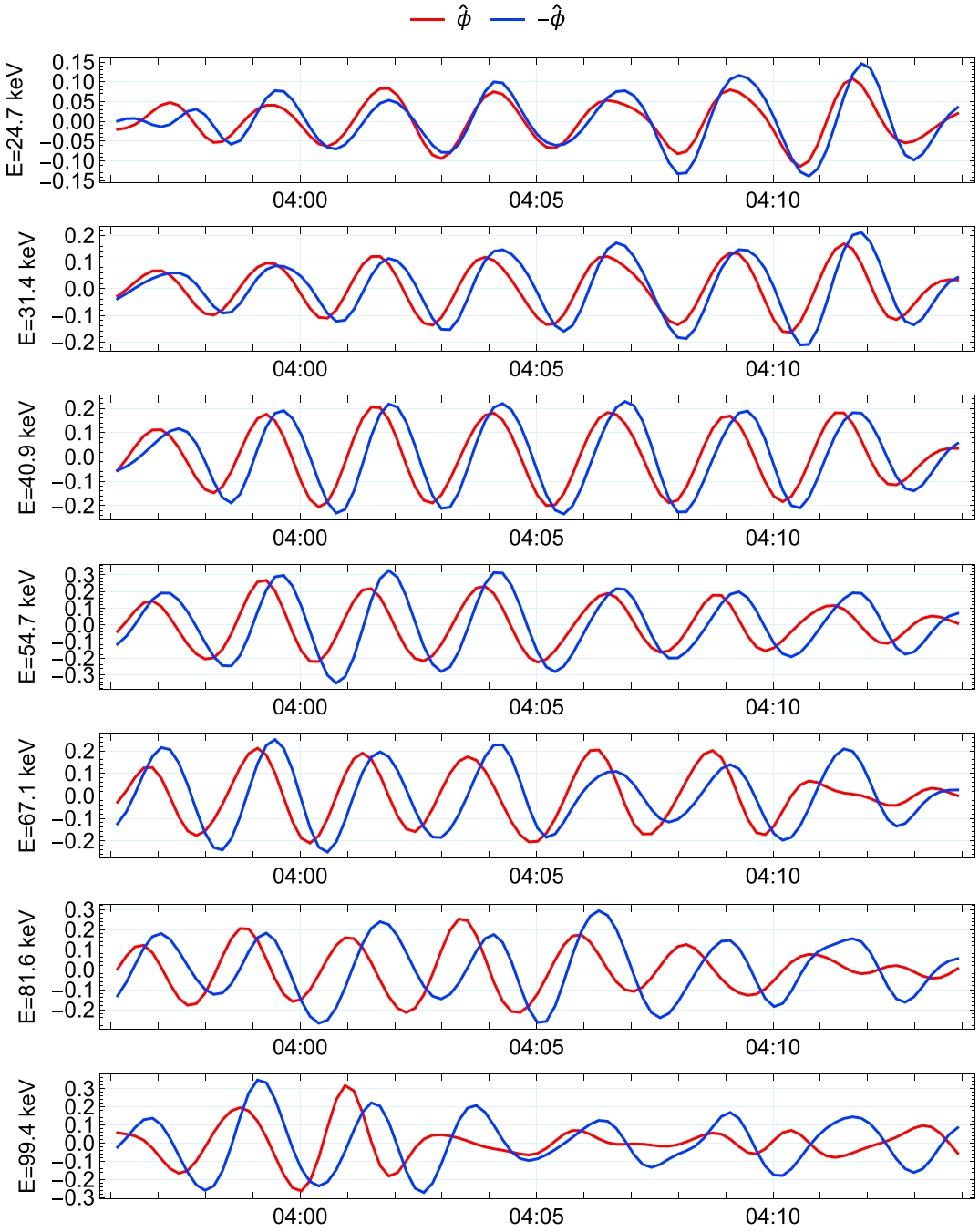

Figure 11. Residual proton fluxes in the $\hat{\phi}$ (red) and $-\hat{\phi}$ (blue) directions shown in Figure 9. These are bandpass filtered between 3 and 11 mHz.

$-\hat{v}$ direction is substantially larger than the flux at the $\hat{v}$ direction, which indicates an inward radial gradient (for fixed energy and pitch angle).

Assuming a westward propagating wave, the flux j that would be seen by the spacecraft can be expressed as

$$j \sim \exp\left[-i2\pi\frac{\rho_L}{\lambda_\perp}\cos(\Omega_{sc}t) - i\omega t\right], \quad (1)$$

where Ω_{sc} is the angular spacecraft spin frequency and $\lambda_\perp = 2\pi/|k_\perp|$. After substituting $\omega = 2\pi \cdot 0.007$ rad/s and $\Omega_{sc} = 2\pi/11$ rad/s into equation (1), the expected spin modulation of protons whose energy corresponds

Table 1. Result of Cross-Correlation Analyses

Energy (keV)	ρ_L (R_E)	r[a]	τ (s)	$k_\perp\rho_L$[b]	$\lambda_\perp$ (R_E)	v_{ph} (R_E/s)	m[c]
24.7	0.0183	0.933	8.7	0.191	0.600	0.00420	−56
31.4	0.0206	0.973	17	0.374	0.346	0.00242	−97
40.9	0.0235	0.988	19.1	0.420	0.352	0.00246	−96
54.7	0.0272	0.975	23.5	0.517	0.330	0.00231	−102
67.1	0.0301	0.907	25.6	0.563	0.336	0.00235	−100
81.6	0.0332	0.855	34.1	0.750	0.278	0.00195	−121
99.4	0.0366	0.794	31.7	0.697	0.330	0.00231	−102

[a]Pearson's correlation coefficient.
[b]Note that $k_\perp\rho_L = \tau\omega/2$. Wave frequency ω is $2\pi \cdot 0.007$ rad s^{-1}.
[c]The negative sign denotes westward ($-\hat{\phi}$) propagation.

to $\rho_L/\lambda_\perp = \frac{1}{16}, \frac{1}{8}, \frac{1}{4}$, and $\frac{1}{2}$ are shown in Figure 10 with the same format as Figure 9. The phase relationship between the fluxes at the two opposite directions described previously is clearly illustrated, confirming westward propagation. In addition, the observed spin modulation patterns shown in Figure 9 appear to be more consistent with the case of $\rho_L/\lambda_\perp \sim 0.1$. The wavelength can be estimated more accurately by examining the phase delay τ between the residual fluxes in the $\hat{\phi}$ and $-\hat{\phi}$ directions. From equation (1), one can obtain the relationship $\tau\omega = 4\pi\rho_L/\lambda_\perp$.

Figure 11 shows residual fluxes (i.e., $\delta \log j$) in the $\hat{\phi}$ (red) and $-\hat{\phi}$ (blue) directions. These are additionally bandpass filtered between 3 and 11 mHz. Immediately noticeable is the phase difference increasing with increasing energy (or increasing $\rho_L/\lambda_\perp$) that is ideally the consequence of $\tau \propto \rho_L$ for fixed ω and $\lambda_\perp$. We carried out cross-correlation analysis on the residual fluxes at two opposite directions. The result is summarized in Table 1. In general, the correlations are very good as suggested by the correlation coefficients greater than 0.8. Assuming that the results of 24.7 and 81.6 keV are outliers, the estimated wavelengths are clustered near $\lambda_\perp = 0.34\,R_E$. Because the distance from Earth's center to the spacecraft is $r_{sc} \approx 5.58\,R_E$ and the spacecraft latitude $\lambda_{sc} \approx 16.5°$, the azimuthal wave number is estimated to be $m \approx -100$ with the negative sign signifying westward ($-\hat{\phi}$) propagation.

4.2. Field Line Structure of Guided Poloidal Wave

In this subsection, we perform eigenmode analysis of the guided poloidal wave [e.g., *Cummings et al.*, 1969] to investigate the field line structure associated with the observed poloidal mode waves. Initially, we assumed the dipole field as the background magnetic field. However, as will be shown, the dipole field line cannot properly represent the stretched field line near the midnight sector. So following *Walker and Pekrides* [1996], we adopt the modified dipole field, which has a few more free parameters that can be adjusted to obtain the desired local field line geometry. The vector potential is given by

$$\mathbf{A} = -k\left(\frac{x}{r^3} + a_1 x + a_2\frac{z^2}{x}\right)\hat{\phi}, \tag{2}$$

where $x = r\cos\lambda$ and $z = r\sin\lambda$ (see Figure 1c); k is constant and has units of, e.g., nT R_E^3; a_1 and a_2 represent the deviation from the dipole field (the first term) and may respectively be interpreted as contributions from ring current and plasma sheet populations [*Walker and Pekrides*, 1996]. This leads to an azimuthally symmetric magnetic field, which is unrealistic globally but sufficient for the local field line representation. The cylindrical components of the magnetic field vector are given by

$$\frac{B_x}{k} = -3\frac{xz}{r^5} + 2a_2\frac{z}{x},\ \frac{B_z}{k} = \frac{x^2 - 2z^2}{r^5} - 2a_1,\ \text{and}\ \frac{B_\phi}{k} = 0. \tag{3}$$

Two of the three unknowns can be determined using the observed magnetic field. One is the constant k, which is not necessary unless eigenfrequencies in real units are needed. The other can be determined from the measured B_x/B_z ratio. The magnetic field averaged between 0400 and 0410 UT is $(B_x, B_\phi, B_z) = (-173.8, -11.29, 86.93)$ nT in Solar Magnetospheric (SM) coordinates. Although B_ϕ has a nonzero value, it is much smaller than B_x so it will be neglected. Then using the distance from Earth's center to the spacecraft $r_{sc} \approx 5.58\,R_E$ and the spacecraft latitude $\lambda_{sc} \approx 16.5°$, a_1 can be determined by $a_1 = 0.25(0.0041 + 0.58a_2)$. A model of the mass density distribution along the field line is also needed to obtain the Alfvén speed V_A.

A commonly used form is $\rho/\rho_0 = (r_0/r)^\alpha$ [e.g., *Motoba et al.*, 2015], where r is the distance from the Earth's center to a point on the field line, ρ is the mass density at r, $r_0 = LR_E$, ρ_0 is the equatorial mass density, and α varies typically between 1 and 6. (A more general form of mass density distributions was also used [*Denton et al.*, 2001, 2004].) Finally, the guided poloidal mode wave equation [*Walker and Pekrides*, 1996] is given by

$$\frac{1}{x}\frac{\mathrm{d}}{\mathrm{d}s}(xE_\phi) - i\omega b_v = 0 \text{ and} \tag{4}$$

$$V_A^2 Bx \frac{\mathrm{d}}{\mathrm{d}s}\left(\frac{b_v}{Bx}\right) - i\omega E_\phi = 0, \tag{5}$$

where s is the arc length of the field line.

Figure 12a shows the dipole field line, the T89 [*Tsyganenko*, 1989] model field line, and the modified dipole field line from equation (3) with $a_2 = -0.004$. The spacecraft location is marked with the solid dot. The modified dipole field line is remarkably consistent with the T89 model field line, whereas the dipole field line failed to represent the stretched field line. We varied a_2 between 0 and −0.02 for the sensitivity test. Increasing a_2 results in the increasing L and the decreasing foot point latitude of the field line. The total L variation between the two extreme cases is less than 0.3, whereas the foot point latitude changes quite significantly. Based on visual inspection, we find that the field line with $a_2 = -0.004$ is most consistent with the T89 field line, which we consider to be the realistic representation of the stretched field line near the midnight sector.

To solve the wave equations (4) and (5), we first assume $a_2 = -0.004$ and $\alpha = 1$. The wave equations are combined to yield a second-order differential equation of E_ϕ

$$\frac{\mathrm{d}}{\mathrm{d}s}\left(\frac{1}{Bx^2}\frac{\mathrm{d}}{\mathrm{d}s}(xE_\phi)\right) = -\frac{\omega^2}{Bx^2 V_A^2} xE_\phi. \tag{6}$$

This is then solved for eigenvalue $\hat{\omega} \equiv \omega r_0/V_{A,0}$ and eigenfunction E_ϕ using the spectral method [*Trefethen*, 2000], where $V_{A,0}$ is the Alfvén speed at the magnetic equator. For the boundary condition, we assume the perfectly conducting ionosphere at 1 R_E for simplicity. Finally, b_v is calculated from equation (4) using E_ϕ. Figures 12b and 12c show the three lowest eigenmode solutions of E_ϕ and b_v along the field line, respectively. Here units are arbitrary, but E_ϕ and b_v are related to each other through equation (4) so they can be directly compared with each other. Because the spacecraft latitude is about 16.5° (vertical dashed line), which is well above the off-equatorial node of the third harmonic mode, amplitudes of E_ϕ are comparable for all three harmonic modes. In contrast, the second and third harmonic modes have an off-equatorial b_v node very close to the spacecraft, leading to significant reduction in b_v amplitudes at the spacecraft for these two harmonic modes. Because the observed waves exhibit relatively strong E_ϕ wave power and relatively weak b_v wave power (Figure 4), it is less likely that the observed poloidal waves are a fundamental mode.

For comparison, Figures 12d and 12e show the eigenmode solutions when the dipole field line is used. The most notable difference is that the off-equatorial nodes in b_v are shifted toward higher latitude. Consequently, b_v has substantial amplitudes at spacecraft latitude for all three harmonic modes. The same calculations have been done for different values of a_2 and α. The primary results are as follows. When a_2 is changed between 0 and −0.02, the latitude of the off-equatorial nodes of all three harmonic modes remains nearly unchanged while the amplitude increases with decreasing a_2. When α increases from 1 to 6, the latitude of the off-equatorial nodes increases significantly (beyond 25° for the second harmonic b_v). This further indicates that α may be close to 1 [e.g., *Motoba et al.*, 2015].

Because the in situ total plasma density is available, one can estimate the average ion mass m_i/m_p given the observed wave frequency of $f \approx 7$ mHz. We calculate m_i/m_p using the eigenfrequencies ($\hat{\omega}$) obtained for several a_2 values with $\alpha = 1$. The results are summarized in Table 2. In the terrestrial magnetosphere, m_i/m_p lies between 1 amu (all protons) and 16 amu (all oxygen ions). Therefore, it is further confirmed that the observed waves cannot be the fundamental mode because the estimated m_i/m_p is far less than 1 in all cases. Furthermore, *Denton et al.* [2011] showed that a typical value of m_i/m_p varies with solar activity but is less than 4 ($m_i/m_p \sim 1$ at solar minimum and ~3.8 at solar maximum). Because the cold plasma density of the plasmaspheric origin was significantly elevated when the waves were detected, it is unlikely that m_i/m_p is larger than 4 unless the cold plasma population contains a substantial concentration of heavier elements than protons. In addition, the HOPE measurements in Figure 5d indicate that m_i/m_p of the three major ion species above 30 eV are about 3 amu. Therefore, we conclude that the poloidal waves observed have the second harmonic standing wave field line structure.

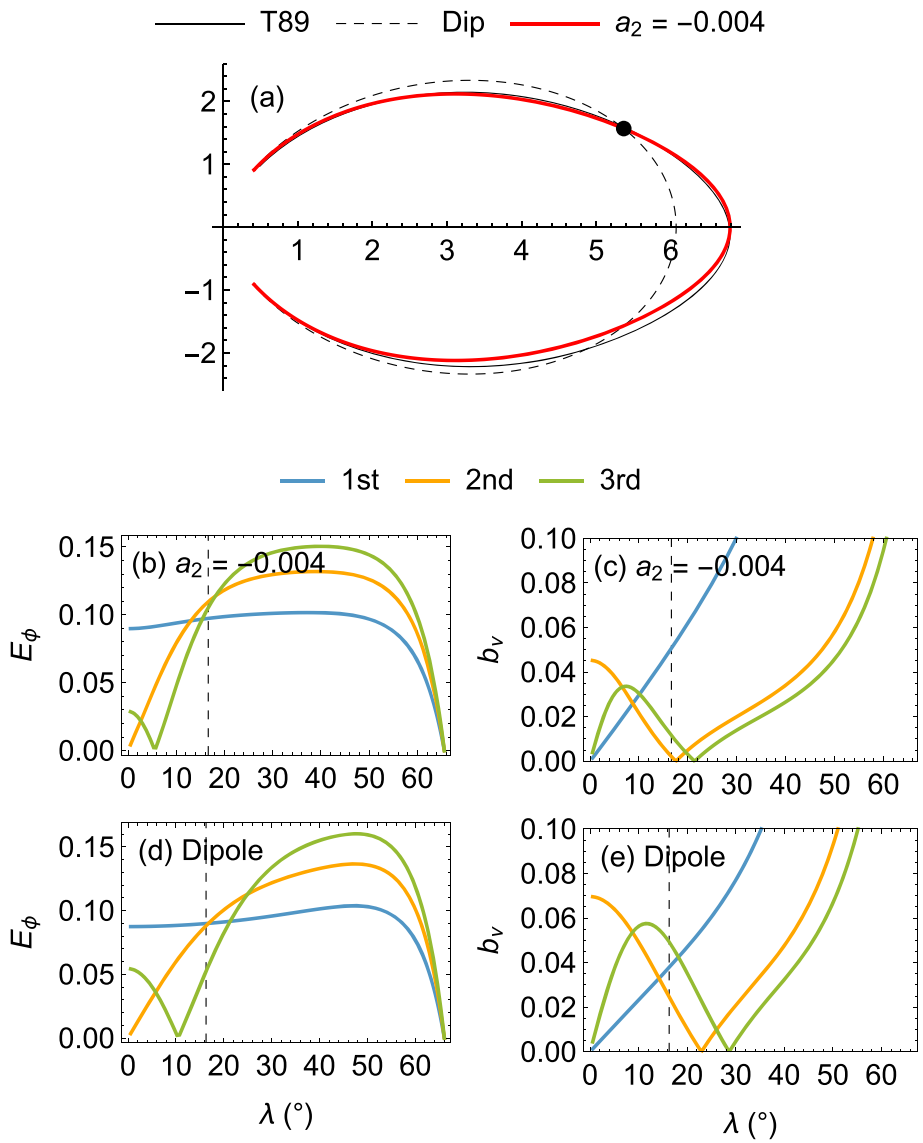

Figure 12. Eigenmode analysis results for three lowest harmonic modes. (a) Comparison of the modified dipole field line for $a_2 = -0.004$ with the dipole and T89 field lines. (b and c) Amplitudes of eigenmodes E_ϕ and b_v along the modified dipole field line with $a_2 = -0.004$ and $\alpha = 1$, and (d and e) amplitudes of eigenmodes E_ϕ and b_v for the dipole field line. The solid dot in Figure 12a and the vertical dashed lines in Figures 12b–12e mark the spacecraft location. The three colored curves in Figures 12b–12e correspond to solutions of the first three harmonic modes as labeled. Unit of E_ϕ is arbitrary, and b_v is related to E_ϕ through equation (4).

This conclusion is also consistent with the GOES-15 observation. As noted in the previous section, because the GOES-15 spacecraft was close to the magnetic equator (Figure 3), the poloidal waves observed by the GOES-15 spacecraft should be an even harmonic mode whose magnetic field fluctuations have an antinode at the equator (see Figure 12c). This argument presumes that the waves seen by GOES-15 are related to the waves seen by RBSP-A. This scenario is discussed in section 5.

4.3. Interpretation of Energetic Proton Pulsations

A theory of charged particle behavior in a transverse low-frequency wave has been given by *Southwood and Kivelson* [1981]. Under the guiding center approximation, the mean rate of change of energy for a particle of charge q is given by $\dot{W} = q\mathbf{E} \cdot \mathbf{V}_d$, where $\mathbf{V}_d$ is the magnetic gradient and curvature drift velocity and $\mathbf{E} \sim E_\phi \exp(i(m\phi - \omega t))\hat{\phi}$. Integration of $\dot{W}$ along the unperturbed drift orbit yields the average energy gain of the particle, δW. Because $\dot{W}$ involves the exponential term whose argument is time dependent, integration introduces a denominator that can become 0 for a particle in resonance with the wave. This singularity is

Table 2. Average Ion Mass Estimates[a]

a_2	Fundamental	Second Harmonic	Third Harmonic
0	0.0251	1.96	4.08
−0.001	0.0364	2.13	4.46
−0.002	0.0476	2.24	4.71
−0.003	0.0583	2.33	4.90
−0.004	0.0686	2.41	5.05
−0.005	0.0783	2.47	5.16
−0.006	0.0875	2.52	5.25
−0.008	0.104	2.60	5.39
−0.01	0.120	2.66	5.50

[a]In atomic mass units (amu). The parameter α is set to 1.

handled by introducing a small imaginary part in the complex frequency ω, which represents temporal wave growth/damping or finite spatial scale of the wave region. The consequence is the energy-dependent phase variation of δW across the resonance energy. In essence, δW of a particle in resonance with the wave can be in-phase or antiphase with the electric field, while δW of a particle whose energy is above or below the resonance energy has a phase shift by ±90° with the electric field [see *Southwood and Kivelson*, 1981; *Glassmeier et al.*, 1999; *Zhou et al.*, 2016 for details]. Therefore, the phase of δW across the resonance energy shifts by 180°. The phase space density variation δf, which is the actual observable quantity, is given by [*Southwood and Kivelson*, 1981]

$$\delta f = -\delta W \left[\left.\frac{\partial f}{\partial W}\right|_{\mu,L} + \frac{\mathrm{d}L}{\mathrm{d}W} \left.\frac{\partial f}{\partial L}\right|_{\mu,W} \right]. \tag{7}$$

Because δf is proportional to δW, the particle fluxes also exhibit the energy-dependent phase variation and the phase reversal across the resonant energy, both of which are a unique feature of the drift-bounce resonant interactions of charged particles with poloidal waves and are often used to determine the resonance energy W_{res} and the m number [e.g., *Claudepierre et al.*, 2013; *Dai et al.*, 2013].

To investigate whether the observed poloidal waves are related to the residual flux pulsations shown in Figures 6b and 6c via the drift-bounce resonance mechanism, Figure 13a compares the residual fluxes of 90° (local) pitch angle protons from the RBSPICE experiment with the azimuthal electric field component E_ϕ. (Note that the residual fluxes and E_ϕ are additionally bandpass filtered between 3 and 11 mHz.)

For more quantitative estimation of the phase differences, we also carried out cross-correlation analysis among the residual fluxes shown in the figure. The result is summarized in Table 3. First, the correlation analysis suggests that the energy of the residual flux that is in phase with E_ϕ is 81.6 keV. Visually from Figure 13a, the 99.4 keV flux also appears to be in phase with E_ϕ, although the phase delay with respect to E_ϕ is about −7°. The resonant energy W_{res} may probably be closer to 81.6 keV than to 99.4 keV. From Table 1, this energy corresponds to $k_\perp \rho_L \approx 0.6$ consistent with the linear theory prediction of the most unstable mode (note that the result of 81.6 keV in Table 1 is an outlier). Second, the phase of the residual flux indeed varies with energy and changes (or appears to change) the sign across the resonant energy. The correlation analysis suggests that the 17.4 keV residual flux lags E_ϕ by almost 90°, while the 99 and 121 keV residual fluxes show the sign of phase reversal. Unfortunately, the count rate drops, the fluctuations become less monochromatic, and amplitudes decrease at the higher energy channels (probably the 121 keV channel may not be reliable), so the 180° phase shift predicted by the theory cannot be confirmed. The fact that $k_\perp \rho_L \gtrsim 1$ at higher energy can be another factor that decreases efficiency of interactions between the electric field and protons with a relatively larger gyroradius. Nevertheless, we point out that the energy-time diagram of the residual fluxes shown in Figure 13b is qualitatively consistent with the same diagrams shown in Figure 4 of *Zhou et al.* [2016] who considered drift resonance.

On the other hand, given the wave properties (second harmonic poloidal mode with $m \approx -100$), one can alternatively calculate the energy of protons that would be in drift-bounce resonance with the observed waves using the drift-bounce resonance condition [e.g., *Southwood*, 1976]:

$$\omega - m\bar{\omega}_d = N\omega_b, \tag{8}$$

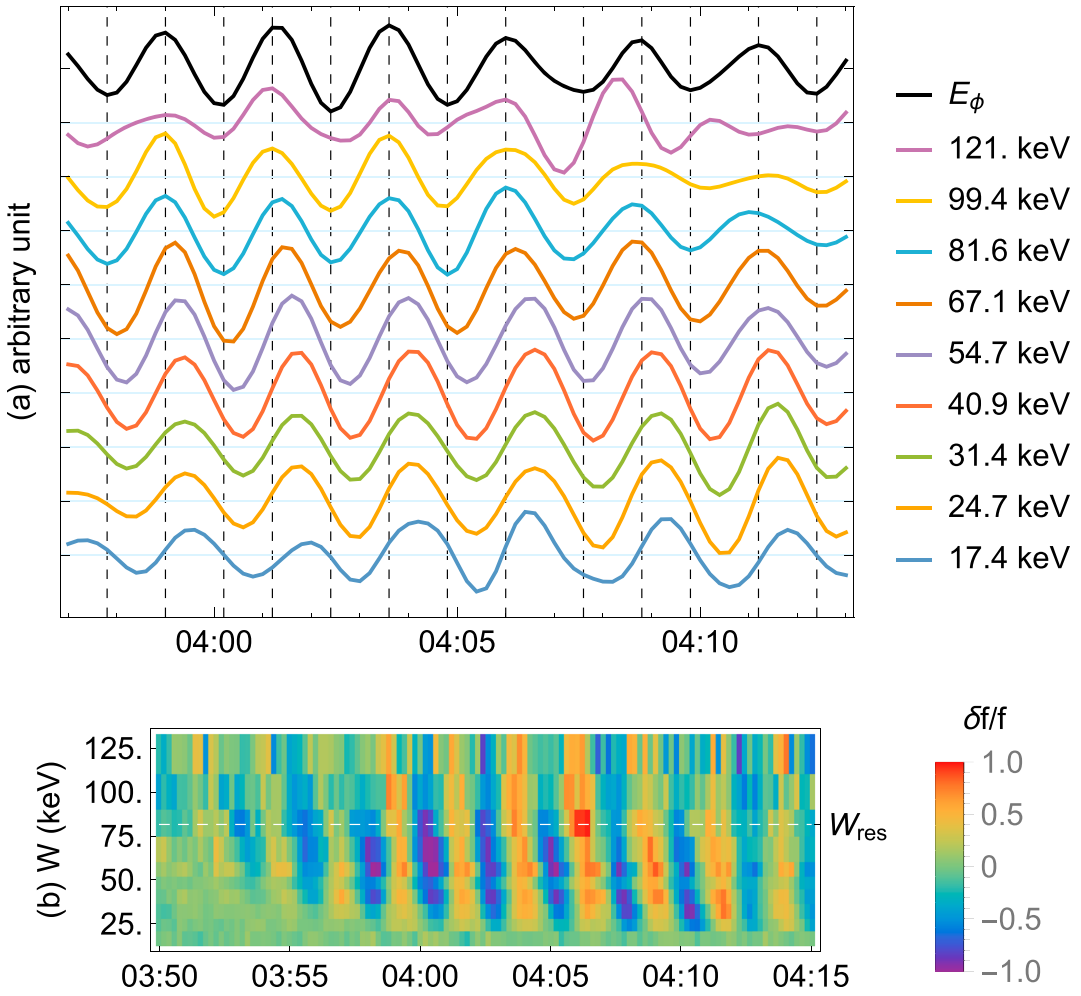

Figure 13. (a) Phase relationship among the local 90° pitch angle proton residual fluxes obtained from the RBSPICE experiment. The oscillations of E_ϕ are also shown as a black curve for reference. The vertical dashed lines mark peaks and valleys in E_ϕ. Units are arbitrary. (b) Two-dimensional plot of the residual proton fluxes shown above (no bandpass filtered). The vertical axis corresponds to the nine energy channels shown in Figure 13a. Color bar unit is arbitrary.

where ω_b and $\bar{\omega}_d$ are the bounce and bounce-averaged drift frequencies, respectively. For the second harmonic mode, $N = \pm 1$ is relevant. Assuming that the Earth's magnetic field is represented by the azimuthally symmetric modified dipole field with $a_2 = -0.004$, we calculate ω_b and $\bar{\omega}_d$ as a function of the particle speed and equatorial pitch angle (Appendix A). Considering the protons mirroring the spacecraft latitude, the calculated resonant energy is about 2.3 keV for $N = 1$ resonance and about 110 keV for $N = -1$ resonance. The former resonance, called low-energy resonance, leads to the condition $\omega \sim \omega_b$, while the latter resonance, called high-energy resonance, leads to the condition $m\bar{\omega}_d \sim \omega_b$ [*Southwood et al.*, 1969]. Although the azimuthally symmetric global magnetic field assumed is certainly unrealistic, the calculated $N = -1$ resonant energy (high-energy resonance) is very close to the energy of protons whose residual flux is in phase with E_ϕ as shown in Figure 13a. Therefore, we conclude that the proton flux modulations shown in Figure 13a are the consequence of drift-bounce wave-particle interactions corresponding to the high-energy resonance.

Proton flux fluctuations corresponding to low-energy resonance ($N = 1$) is not clear. As shown in Figure 5b and more clearly in Figure 6c, the proton fluxes with energy of a few keV were nearly static until 0412 UT. After this time, the fluxes exhibited nearly sinusoidal oscillations that extended to the energy as low as 1 keV. However, the waves became less monochromatic and amplitudes were subsequently diminished. It could be that the lower energy protons did not respond to the poloidal waves observed and some other mechanisms modulated the later fluctuations, or that they did interact with the waves but it took a while for the signal to be detected.

Table 3. Phase Relationship Between E_ϕ and Energetic Protons

W (keV)	r[a]	Phase Delay[b](deg)
17.4	0.883	85.7
24.7	0.907	68.0
31.4	0.926	65.5
40.9	0.953	60.5
54.7	0.958	45.4
67.1	0.931	20.16
81.6	0.953	0.00
99.4	0.941	−7.56
121	0.682	−30.2

[a]Pearson's correlation coefficient.
[b]A positive phase indicates that E_ϕ is leading the residual flux.

4.4. Source of Free Energy

So far, we have observationally confirmed that the observed waves are propagating westward with $|m| \approx 100$, have the second harmonic standing wave structure, have finite compressional magnetic perturbations, and interact with energetic ($\lesssim$100 keV) protons via the high-energy drift-bounce resonance. A theory that takes into account the finite Larmor radius effect also predicts that the second harmonic mode with $k_\perp \rho_L \sim 0.5$ is the most unstable solution [*Chen and Hasegawa*, 1988, 1991]. The theory further suggests that the instability can be fed by the hot ion pressure gradient directed radially inward via the high-energy drift-bounce resonance mechanism. In this subsection, we provide observational support that protons in high-energy resonance can have destabilizing effects via drift-bounce resonance as the theory predicts.

Southwood et al. [1969] provided a general picture of the drift-bounce wave-particle interaction mechanism in analogy to quasi-linear theory of cyclotron resonant interactions. Particles diffuse along unique curves in *W*-*L* space from regions of high density to low-density regions. Waves can be destabilized if particles lose energy as they diffuse. Formally, the instability condition is given by

$$\frac{\mathrm{d}f}{\mathrm{d}W} = \left.\frac{\partial f}{\partial W}\right|_{\mu,L} + \frac{\mathrm{d}L}{\mathrm{d}W}\left.\frac{\partial f}{\partial L}\right|_{\mu,W} > 0, \tag{9}$$

where f is the particle distribution function and μ is the first invariant. For protons drifting in the dipole magnetic field, $\mathrm{d}L/\mathrm{d}W$ is approximately given by [*Southwood et al.*, 1969]

$$\frac{\mathrm{d}L}{\mathrm{d}W} \approx \frac{mL^2}{eB_E\omega R_E^2}, \tag{10}$$

where e is the elementary charge and B_E is the equatorial magnetic field magnitude at the Earth's surface. This suggests that either bump-on-tail distributions with $\partial f/\partial W > 0$ [e.g., *Hughes et al.*, 1978a; *Glassmeier et al.*, 1999; *Baddeley et al.*, 2004, 2005; *Wilson et al.*, 2006; *Liu et al.*, 2013] or distributions with inward gradients, $\partial f/\partial L < 0$ [*Takahashi et al.*, 1990; *Dai et al.*, 2013], can destabilize westward propagating waves via drift-bounce resonance.

Figure 14a shows the phase space density profile of 90° (local) pitch angle protons averaged between 0357 and 0413 UT. Measurements from three particle experiments are shown. The HOPE fluxes have been raised by a factor of 2. High-energy ion fluxes measured by the HOPE experiment are often underestimated [*Kistler et al.*, 2016], and an increase by a factor of 2 generally brings them into agreement with the low-energy RBSPICE fluxes. There is also discrepancy between the MagEIS and RBSPICE (ToFxE) measurements at the high-energy tail. We neglect this part because the flux level there is low. Although the particle flux j is related to the phase space density f by $f = j/p^2$, where p is the particle momentum [e.g., *Roederer*, 1970], we show j/W as a proxy for f for convenience. As far as the analysis concerned here, the constant scale factor is not important.

To examine whether the waves can gain energy from the protons in high-energy resonance, we test the sign of $\mathrm{d}f/\mathrm{d}W$ evaluated at the resonant energy (that is, $W_{\mathrm{res}} \approx 81.6$ keV). Apparently, $\partial f/\partial W < 0$ as shown in Figure 14a. To be more quantitative, we fit a straight line to the phase space density near the resonant energy and then calculate $\partial f/\partial W$ from the slope of the line. On the other hand, we approximate $\partial f/\partial L$ by finite

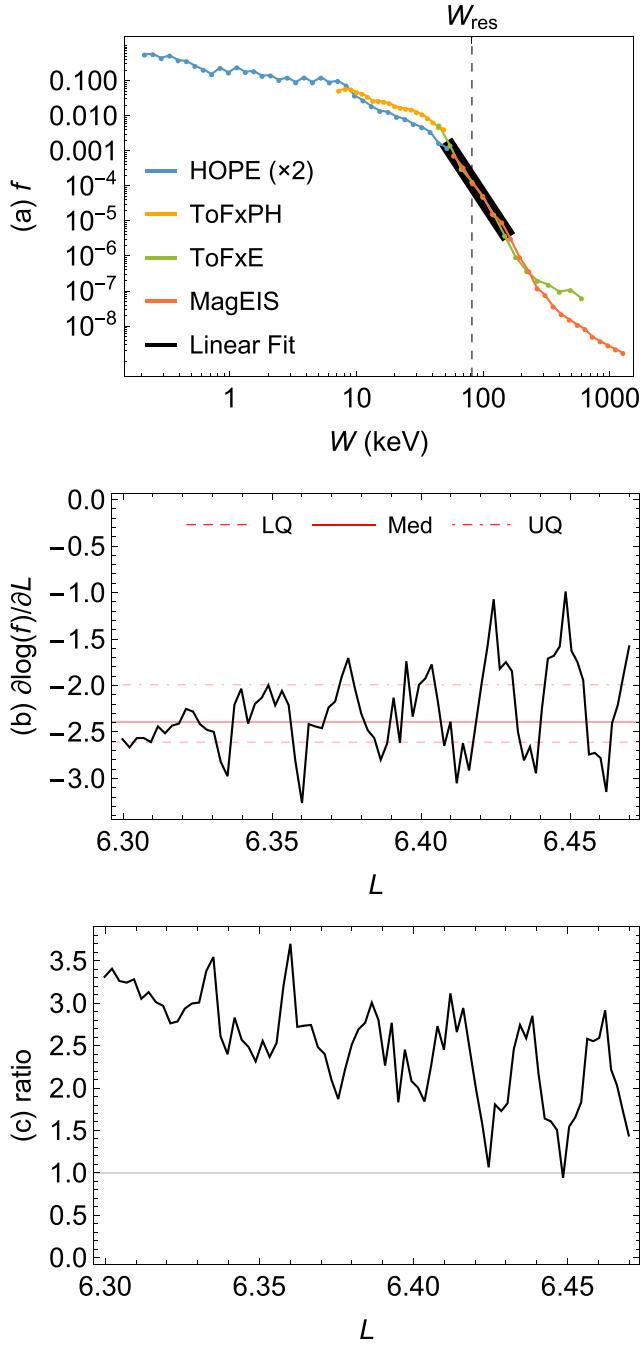

Figure 14. (a) Phase space density profile of local 90° pitch angle protons obtained from three particle experiments as a function of energy. The phase space density from HOPE is raised by a factor of 2. The resonant energy is marked by the vertical dashed line. The black line represents a linear fit of the phase space density near $W = W_{res}$. Unit of phase space density is 1/cm^2 s sr eV^2. (b) Radial gradient of the phase space density of local 90° pitch angle protons (that is, $\partial f/\partial L|_{\mu,W}$) evaluated at the resonant energy. (c) Ratio of $\frac{dL}{dW}\frac{\partial f}{\partial L}$ to $\left|\frac{\partial f}{\partial W}\right|$ evaluated at the resonant energy.

difference while keeping μ and W constant. The result is shown in Figure 14b. The plot of $\partial f/\partial L$ is somewhat oscillatory because the 20 min average does not remove wave modulation completely. For guidance, the median value as well as the lower and upper quartiles are marked with the horizontal lines. The gradient of the phase space density is radially inward ($\partial f/\partial L < 0$) as expected from Figure 9. Because the m number is negative, $(dL/dW)(\partial f/\partial L)$ becomes positive. Figure 14c shows the ratio of $(dL/dW)(\partial f/\partial L)$ to $|\partial f/\partial W|$. Because this ratio greater than unity means $df/dW > 0$, this result suggests that the protons in high-energy resonance can provide free energy.

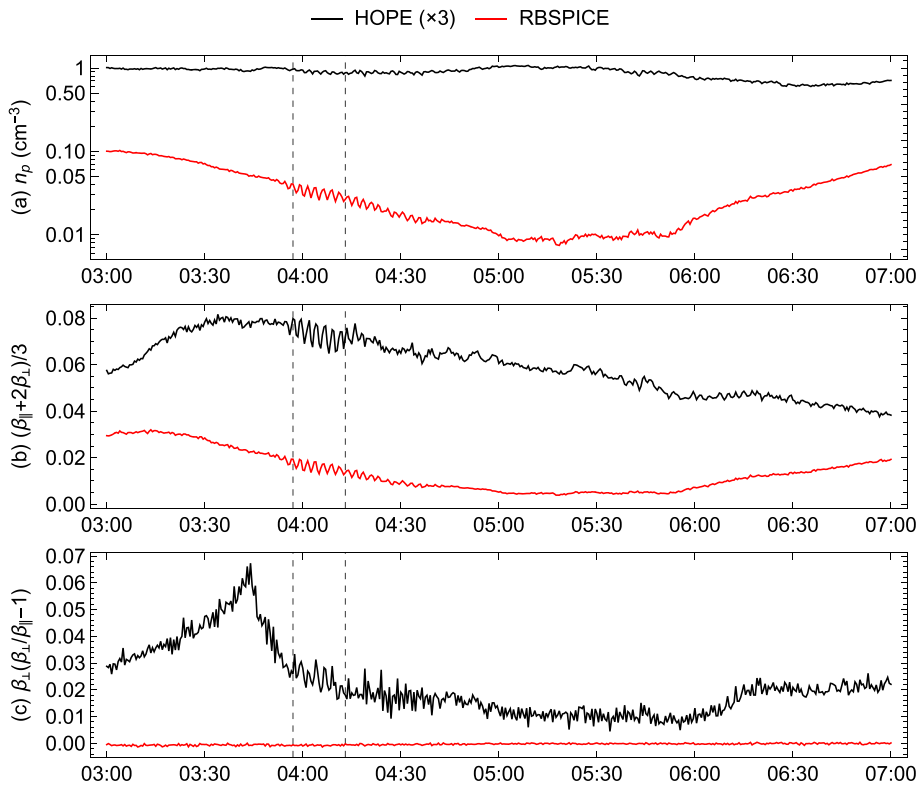

Figure 15. (a) Proton number densities, (b) proton betas, and (c) mirror mode instability thresholds obtained from the HOPE and RBSPICE measurements. As for the HOPE processing, proton fluxes of energy above 30 eV are used. The fluxes are additionally raised by a factor of 2. As for the RBSPICE processing, proton fluxes of energy above 50 keV are used.

It should be noted that there is another resonance at $N = 1$ (low-energy resonance) which provides stabilizing effects if $\partial f/\partial W < 0$ [*Southwood*, 1976; *Chen and Hasegawa*, 1988]. It is in fact the competition between the destabilizing effects by the $N = -1$ resonance and the stabilizing effects by the $N = 1$ resonance that determines ultimate wave growth. It is generally difficult to quantitatively determine whether growth by the high-energy resonant protons outweighs damping by the low-energy resonant ones. Besides, the energy corresponding to $N = 1$ resonance cannot be determined in the same way as the high-energy resonance. However, for an adiabatically injected background plasma distribution for which $\partial f/\partial L|_{\mu,J} \approx 0$ where J is the second invariant, one requires $\omega < \omega_{bT}$ for instability by the high-energy resonance, where the subscript T denotes a thermal value [*Southwood*, 1976; *Chen and Hasegawa*, 1988]. Because the local field line model is assumed to be realistic, one can determine the bounce frequency more or less accurately. We calculate the proton thermal speed ($v_{\mathrm{th}} = \sqrt{T/m_p}$) by taking into account both the HOPE and RBSPICE measurements. For this event, $\omega_{bT}/\omega \approx 1.13$, so the instability condition is still satisfied at least for an adiabatic distribution.

As described in section 1, β is an important quantity that determines the wave characteristics and the instability source. Figure 15 shows the proton number density, proton β, and the mirror mode instability criterion [*Hasegawa*, 1969]. The black traces account for protons of energy from above 30 eV to below 50 keV measured by the HOPE experiment (with the factor-of-2 adjustment), while the red traces account for protons of energy above 50 keV measured by the RBSPICE experiment (only the ToFxE product). During the whole period, β is on the order of 0.1 (mostly contributed by the low-energy protons) and the mirror instability condition, $\sum_j \beta_{\perp j}(\beta_{\perp j}/\beta_{\parallel j} - 1) > 1$, is far from being met, where the summation is done over the particle populations. Therefore, it is unlikely that the drift mirror instability can be a viable mechanism for the wave generation. On the other hand, small but finite β can cause finite coupling between transverse and compressional Alfvén modes, leading to the finite compressional magnetic field perturbations observed [e.g., *Chen and Hasegawa*, 1991; *Walker and Pekrides*, 1996].

Note that the analysis here is rather qualitative. For instance, the dipole magnetic field assumption has been made in dL/dW, and of course, the energetic proton distribution may not be adiabatic. Nevertheless, the data

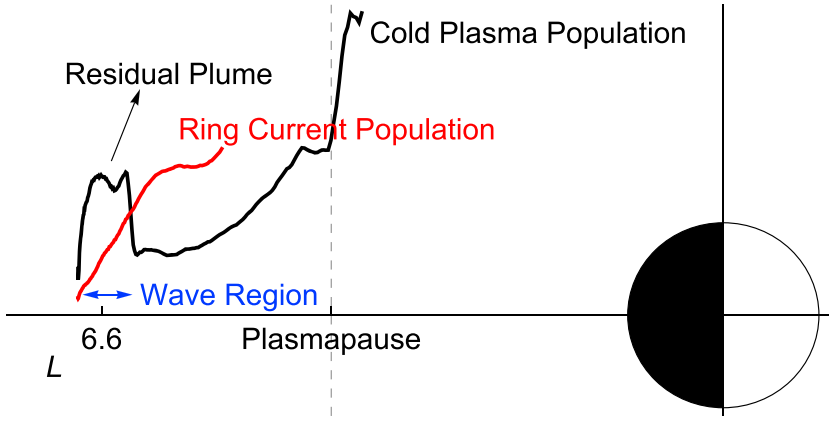

Figure 16. Schematic diagram of the wave excitation region relative to the outer edge of ring current and the residual plasmaspheric plume.

suggest that the inward radial gradients of protons in high-energy resonance could have provided free energy as theory predicts.

5. Discussions

Physical interpretation of the wave generation from an inward gradient of the ring current population is that the resonant protons execute radial excursion in *L* while they lose energy [*Southwood*, 1976]. This indicates that the observation was made at the outer edge of ring current that overlapped with the residual plume region.

Figure 16 schematically illustrates the radial structure of the residual plume and the ring current for this event. The cold plasma profile (in linear scale) is based on the real data in Figure 5c (taken from the total electron density in the outbound pass) while the ring current profile, which is based on the energetic proton number density in Figure 15a, is an illustration of the outer edge of the ring current. The wave active region is where these two regions overlap. Perhaps this region is also where the energetic ring current population provides free energy while the enhanced cold plasma density lowers the field line resonance frequency and wave damping [*Southwood*, 1976; *Chen and Hasegawa*, 1988; *Engebretson et al.*, 1992; *Liu et al.*, 2013; *Dai et al.*, 2015]. *Vetoulis and Chen* [1994, 1996] showed that radial localization of poloidal waves can occur in a region where the poloidal Alfvén frequency exhibits a local minimum (dip) with respect to *L* and where it is lower than the toroidal frequency. These authors suggested that sufficiently strong earthward pressure gradient (the outer edge of the ring current) can lead to such a dip. *Denton et al.* [2003] tested whether poloidal waves occur in association with a dip in the poloidal frequency and found instead that it may result from the *L* dependence of the background density or magnetic field. For the present event, localization by the background density variation appears to be the most likely scenario. Qualitatively, the poloidal frequency is related to the Alfvén speed ($\omega \sim k_{\|} V_A$) [e.g., *Denton et al.*, 2003]. Therefore, the sudden enhancement of the background plasma density in our event can create a dip in the poloidal frequency, trapping the poloidal waves. It is also possible that the inward gradient also assists in this localization.

Figure 17 shows the wave active periods obtained from RBSP-A (Figure 4) and GOES-15 (Figure 8). (No monochromatic poloidal waves were detected by RBSP-B.) GOES-13 was about 4 h ahead of GOES-15, but magnetometer data were not available on 20 May 2013. In addition, magnetometer data on the previous day did not show noticeable wave activity (not shown). On the other hand, proton fluxes of ~95 keV from GOES-15 showed pulsations with the same frequency as the magnetic field pulsations simultaneously detected in Figure 8. So we examined proton fluxes from GOES-13 and found a short period of flux pulsations that are consistent with those from GOES-15 and a substantial reduction in the flux level thereafter (not shown). This period is shown in the figure for GOES-13. Note that all orbits are projected onto the magnetic equator along the dipole field line. Interestingly, the (dipole) *L* shell of GOES-13 is about 6.8 while the *L* shell of GOES-15 is about 6.6. This is because the orbit of GOES-13 was located farther northward than GOES-15. Consequently, the orbital configurations were such that the orbit of GOES-15 overlaps that of RBSP-A while the orbit of GOES-13 is located beyond the apogee of RBSP-A at which the wave power reduced significantly (Figure 4).

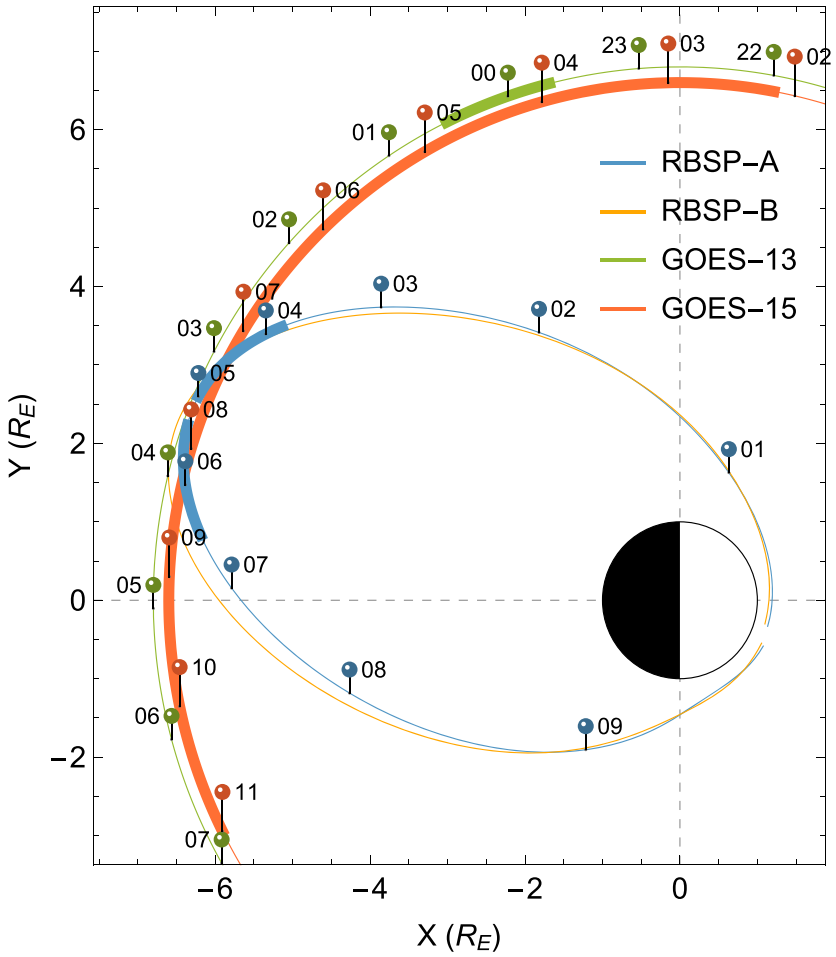

Figure 17. Wave active period registered by RBSP-A, RBSP-B, GOES-13, and GOES-15. The thin curves show the spacecraft orbits projected along the dipole field line onto the magnetic equator. The wave active periods are marked by the thick curves. The vertical pins mark every hour in UT denoted next. The UT hours less than 12 h are on 20 May 2013 and greater than 12 h on the previous day.

If temporal effects can be ignored (due perhaps to the quiet geomagnetic condition), persistent wave activity detected by GOES-15 may indicate that the wave active region shown in Figure 16 was quite wide longitudinally covering roughly the dusk-midnight quadrant as shown in Figure 17. Particularly, the fact that the frequency varies only gradually indicates that the mass density variation is gradual as well; hence, the spacecraft was within the plume. On the other hand, the orbit of GOES-13 was located outside the plume for the most of time, delineating the outer edge of the wave active region. Therefore, it may be possible that the radial structure shown in Figure 16 is extended roughly from dusk to midnight.

This view of the global wave active region is supported by the previous statistical study. As introduced in section 1, *Engebretson et al.* [1992] statistically investigated the ULF waves detected in the noon and dusk sectors and found features that are in good agreement with our event. Particularly, they showed that the waves have a wide longitudinal extent ranging from 1.5 to 8 h in magnetic local time and a narrow extent in L, occur during geomagnetically quiet times usually after geomagnetic storms, and are found in regions far outside the plasmasphere but of density characteristic of the outer plasmasphere ($n_e \sim 10$ cm^{-3}). Their Figures 5, 8, 12, 14, and 15, which show the wave active periods superimposed onto the spacecraft orbits, are very consistent with our Figure 17 apart from the local time of wave occurrence. They further suggested that the free energy of ~100-keV ring current population drives the observed waves through drift-bounce resonant interactions, while the local plasma density increases are the immediate cause of wave onset by altering the field line resonance conditions. We suggest that the results of the present paper provide observational

evidence for this scenario. The role of the background plasma density in the wave onset and the storm time behavior of the plasmaspheric plume may be a possible explanation for the reported rare occurrence of nightside poloidal waves.

6. Summary

We have analyzed an observation by Van Allen Probes of radially polarized low-frequency hydromagnetic waves and associated energetic proton pulsations. The event occurred during geomagnetically quiet time 2 days after a minor geomagnetic storm. Narrowband ULF waves were registered in the premidnight sector by RBSP-A when it was passing through an enhanced density region, perhaps a residual plume, located near geosynchronous orbit. The other spacecraft, RBSP-B, which passed through this region earlier, only detected broadband noise, however.

Despite the measurements from only one spacecraft, we were able to determine various wave properties. Particularly, we were able to unambiguously determine the azimuthal wave number m by examining spin modulation of the energetic proton fluxes caused by the finite Larmor radius effect. Furthermore, we fitted the stretched field line model to data to determine the field line structure of the standing wave. Our findings are as follows: (1) the waves are a second harmonic poloidal mode propagating westward with the azimuthal wave number estimated to be $|m| \approx 100$, (2) the magnetic field fluctuations have finite compressional component associated with small but finite beta of about 0.1, (3) the energetic proton fluxes in the energy range from above 10 to 100 keV exhibit wave-modulated pulsations and energy-dependent phase delays relative to the azimuthal component of the electric field providing evidence for drift-bounce resonance, (4) these protons are in high-energy resonance with the resonant energy about 80 keV, (5) the wavelength in the azimuthal direction is comparable with the Larmor radius of the resonant protons such that $k_\perp \rho_L \sim 0.6$, and (6) the inward radial gradient of ring current protons may have provided free energy to excite the observed waves via the drift-bounce resonance mechanism. These wave properties are consistent with those of the most unstable mode solution predicted by *Chen and Hasegawa* [1988, 1991].

The source of free energy and the existence of the residual plume indicate that the wave active region is where the plume, which is narrow in the radial direction (less than 1 R_E), overlaps with the outer edge of ring current. In addition, based on the available observations at geosynchronous orbit, we were able to provide a global context of the wave active region. Particularly, persistent wave activity detected by one of the geosynchronous satellites suggests that the excitation region narrow in L can have a wide longitudinal extent. It appears that this type of ULF wave commonly occurs in the magnetospheric plasma during geomagnetically quiet times as the statistical study by *Engebretson et al.* [1992] suggested. Finally, the important role of the background plasma density on wave onset is confirmed.

Appendix A: Angular Bounce and Drift Frequencies for Modified Dipole Field

The bounce and bounce-averaged drift frequencies are important to examine the drift-bounce resonant condition given in equation (8). For the dipole field model, they are readily available [e.g., *Hamlin et al.*, 1961; *Roederer*, 1970]. We follow the description in the first two chapters of *Roederer* [1970] and briefly describe how these characteristic frequencies can be obtained for the modified dipole model used here.

Following *Walker and Pekrides* [1996] and referencing the coordinate system in Figure 1, one can choose the ν coordinate:

$$\nu = k\left(\frac{\cos^2\lambda}{r} + a_1 r^2\cos^2\lambda + a_2 r^2 \sin^2\lambda\right). \tag{A1}$$

It is useful to use the (r, λ) coordinate system. The magnetic field components in this coordinate system are given by

$$\frac{B_r}{k} = -2\sin\lambda\left(\frac{1}{r^3} + a_1 - a_2\right) \text{ and } \frac{B_\lambda}{k} = \cos\lambda\left(\frac{1}{r^3} - 2a_1 - 2a_2\tan^2\lambda\right). \tag{A2}$$

The coordinates (r, λ) of a field line are determined by $\nu(r, \lambda) = \nu_{sc}$ for a given reference point, e.g., at a spacecraft location (r_{sc}, λ_{sc}), and thus

$$\cos^2\lambda = -\frac{r(a_2 r^2 - \nu_{sc})}{1 + (a_1 - a_2)r^3}, \tag{A3}$$

where $\nu_{sc} = \nu(r_{sc}, \lambda_{sc})$. Using differential equation of a field line $rd\lambda/B_\lambda = dr/B_r$, the element of field line arc length is given by

$$ds = \sqrt{dr^2 + r^2 d\lambda^2} = \sqrt{1 + B_\lambda^2/B_r^2}\,dr, \tag{A4}$$

where λ is determined by equation (A3). Following *Roederer* [1970], the integral

$$S_b = 2\int_0^{s_m} \frac{ds}{\sqrt{1 - B(s)/B_m}} = 2\int_{r_m}^{r_0} \sqrt{\frac{1 + B_\lambda^2(r)/B_r^2(r)}{1 - B(r)/B_m}}\,dr \tag{A5}$$

is related to the bounce frequency ω_b by $w_b \equiv \omega_b r_0/v = \pi r_0/S_b$, where v is the particle velocity, $r_0 = LR_E$, r_m is the distance from the center of the Earth to the mirror point, $B = \sqrt{B_r^2 + B_\lambda^2}$ and $B_m = B(r_m)$, and w_b is the normalized bounce frequency. Here hemispheric symmetry of the field line is assumed.

The gradient-curvature drift velocity [*Roederer*, 1970] of a proton is given by

$$\mathbf{V}_{CG} = -\frac{m_p v^2}{2eBR_c}(2 - \sin^2\alpha)\hat{\mu} \times \hat{\nu}, \tag{A6}$$

where R_c is the radius of curvature of the field line, α is the pitch angle, and m_p and e are the proton rest mass and the elementary charge, respectively. The curvature radius can be obtained from the relation $(\hat{\mu} \cdot \nabla)\hat{\mu} = -\hat{\nu}/R_c$ [e.g., *Walker*, 1987] and $(\hat{\mu} \cdot \nabla)\hat{\mu}$ is given by

$$(\hat{\mu} \cdot \nabla)\hat{\mu} = \left(b_r \frac{\partial b_r}{\partial r} + \frac{b_\lambda}{r}\frac{\partial b_r}{\partial \lambda} - \frac{b_\lambda^2}{r}\right)\hat{r} + \left(b_r \frac{\partial b_\lambda}{\partial r} + \frac{b_\lambda}{r}\frac{\partial b_\lambda}{\partial \lambda} + \frac{b_r b_\lambda}{r}\right)\hat{\lambda}, \tag{A7}$$

where $b_r = B_r/B$ and $b_\lambda = B_\lambda/B$. Inserting (A6) into the bounce-averaged gradient-curvature drift speed [*Roederer*, 1970]

$$\langle V_{CG} \rangle = \frac{2}{S_b}\int_{r_m}^{r_0} \frac{V_{CG}}{r\cos\lambda/r_0} \sqrt{\frac{1 + B_\lambda^2(r)/B_r^2(r)}{1 - B(r)/B_m}}\,dr, \tag{A8}$$

the bounce-averaged drift frequency $\bar{\omega}_d$ is given by

$$\bar{w}_d \equiv \frac{2ek}{m_p v^2 r_0}\bar{\omega}_d = \frac{2}{S_b r_0}\int_{r_m}^{r_0} \frac{2 - B(r)/B_m}{r\cos\lambda R_c B(r)/k} \sqrt{\frac{1 + B_\lambda^2(r)/B_r^2(r)}{1 - B(r)/B_m}}\,dr, \tag{A9}$$

where $\bar{w}_d$ is the normalized bounce-averaged drift frequency. Note that w_b and $\bar{w}_d$ are determined solely from the field line geometry. In this study, the integrals of (A5) and (A9) are evaluated numerically.

Acknowledgments

RBSPICE data are available at http://rbspice.ftecs.com/Data.html. EMFISIS data are available at http://emfisis.physics.uiowa.edu/data/index. ECT/HOPE data are available at http://www.rbsp-ect.lanl.gov/science/DataDirectories.php. EFW data are available at http://www.space.umn.edu/rbspefw-data/. GOES data are avaliable at http://www.ngdc.noaa.gov/stp/satellite/goes/dataaccess.html. The *SYM-H* and *AE* indices were provided by the Data Analysis Center for Geomagnetism and Space Magnetism in Kyoto, Japan. OMNI solar wind data were provided through OMNI Web Plus (http://omniweb.gsfc.nasa.gov/). The RBSPICE instrument was supported by The Johns Hopkins University Applied Physics Laboratory (JHU/APL) subcontract 937836 to the New Jersey Institute of Technology under NASA Prime contract NAS5-01072. The EMFISIS instrument was supported on JHU/APL contract 921647 under NASA Prime contract NAS5-01072. The ECT suite was supported by RBSP-ECT funding provided by JHU/APL contract 967399 under NASA's Prime contract NAS5-01072. The work by the EFW team was conducted under JHU/APL contract 922613 (RBSP-EFW). The work by K.T. was supported by NASA grant NNX14AB97G. Part of the work by K.M. was supported by NASA grant NNX16AM98G.

References

Baddeley, L., T. Yeoman, D. Wright, K. Trattner, and B. Kellet (2004), A statistical study of unstable particle populations in the global ring current and their relation to the generation of high ULF waves, *Ann. Geophys.*, *22*, 4229–4241, doi:10.5194/angeo-22-4229-2004.

Baddeley, L. J., T. K. Yeoman, D. M. Wright, K. J. Trattner, and B. J. Kellet (2005), On the coupling between unstable magnetospheric particle populations and resonant high *m* ULF wave signatures in the ionosphere, *Ann. Geophys.*, *23*, 567–577, doi:10.5194/angeo-23-567-2005.

Blake, J. B., et al. (2013), The Magnetic Electron Ion Spectrometer (MagEIS) Instruments aboard the Radiation Belt Storm Probes (RBSP) Spacecraft, *Space Sci. Rev.*, *179*, 383–421, doi:10.1007/s11214-013-9991-8.

Chen, L., and A. Hasegawa (1988), On magnetospheric hydromagnetic waves excited by energetic ring-current particles, *J. Geophys. Res.*, *93*, 8763–8767, doi:10.1029/JA093iA08p08763.

Chen, L., and A. Hasegawa (1991), Kinetic theory of geomagnetic pulsations. I—Internal excitations by energetic particles, *J. Geophys. Res.*, *96*, 1503–1512, doi:10.1029/90JA02346.

Cheng, C. Z., and Q. Qian (1994), Theory of ballooning-mirror instabilities for anisotropic pressure plasmas in the magnetosphere, *J. Geophys. Res.*, *11,193–11,210*, 99, doi:10.1029/94JA00657.

Claudepierre, S. G., et al. (2013), Van Allen Probes observation of localized drift resonance between poloidal mode ultra-low frequency waves and 60 keV electrons, *Geophys. Res. Lett.*, *40*, 4491–4497, doi:10.1002/grl.50901.

Crabtree, C., and L. Chen (2004), Finite gyroradius theory of drift compressional modes, *Geophys. Res. Lett.*, *31*, L17804, doi:10.1029/2004GL020660.

Cummings, W. D., R. J. O'Sullivan, and P. J. Coleman Jr. (1969), Standing Alfvén waves in the magnetosphere, *J. Geophys. Res.*, *74*, 778–793, doi:10.1029/JA074i003p00778.

Dai, L., et al. (2013), Excitation of poloidal standing Alfvén waves through drift resonance wave-particle interaction, *Geophys. Res. Lett.*, *40*, 4127–4132, doi:10.1002/grl.50800.

Dai, L., et al. (2015), Storm time occurrence and spatial distribution of Pc4 poloidal ULF waves in the inner magnetosphere: A Van Allen Probes statistical study, *J. Geophys. Res. Space Physics*, *120*, 4748–4762, doi:10.1002/2015JA021134.

Denton, R. E., M. R. Lessard, R. Anderson, E. G. Miftakhova, and W. J. Hughes (2001), Determining the mass density along magnetic field lines from toroidal eigenfrequencies: Polynomial expansion applied to CRRES data, *J. Geophys. Res.*, *106*(A12), 29,915–29,924, doi:10.1029/2001JA000204.

Denton, R. E., M. R. Lessard, and L. M. Kistler (2003), Radial localization of magnetospheric guided poloidal Pc 4–5 waves, *J. Geophys. Res.*, *108*, 1105, doi:10.1029/2002JA009679.

Denton, R. E., K. Takahashi, R. R. Anderson, and M. P. Wuest (2004), Magnetospheric toroidal Alfvén wave harmonics and the field line distribution of mass density, *J. Geophys. Res.*, *109*, A06202, doi:10.1029/2003JA010201.

Denton, R. E., M. F. Thomsen, K. Takahashi, R. R. Anderson, and H. J. Singer (2011), Solar cycle dependence of bulk ion composition at geosynchronous orbit, *J. Geophys. Res.*, *116*, A03212, doi:10.1029/2010JA016027.

Dettrick, S., L.-J. Zheng, and L. Chen (2003), Kinetic theory of geomagnetic pulsations: 4. Hybrid gyrokinetic simulation of drift-bounce resonant excitation of shear Alfvén waves, *J. Geophys. Res.*, *108*, 1150, doi:10.1029/2002JA009650.

Elkington, S. R. (2006), A review of ULF interactions with radiation belt electrons, in *Magnetospheric ULF Waves: Synthesis and New Directions, Geophys. Monogr. Ser.*, vol. 169, edited by K. Takahashi et al., pp. 177–193, AGU, Washington, D. C.

Elkington, S. R., M. K. Hudson, and A. A. Chan (1999), Acceleration of relativistic electrons via drift-resonant interaction with toroidal-mode Pc-5 ULF oscillations, *Geophys. Res. Lett.*, *26*(21), 3273–3276, doi:10.1029/1999GL003659.

Elkington, S. R., M. K. Hudson, and A. A. Chan (2003), Resonant acceleration and diffusion of outer zone electrons in an asymmetric geomagnetic field, *J. Geophys. Res.*, *108*(A3), 1116, doi:10.1029/2001JA009202.

Engebretson, M. J., D. L. Murr, K. N. Erickson, R. J. Strangeway, D. M. Klumpar, S. A. Fuselier, L. J. Zanetti, and T. A. Potemra (1992), The spatial extent of radial magnetic pulsation events observed in the dayside near synchronous orbit, *J. Geophys. Res.*, *97*, 13,741–13,758, doi:10.1029/92JA00992.

Funsten, H., et al. (2013), Helium, Oxygen, Proton, and Electron (HOPE) Mass Spectrometer for the Radiation Belt Storm Probes Mission, *Space Sci. Rev.*, *179*(1–4), 423–484, doi:10.1007/s11214-013-9968-7.

Georgiou, M., I. A. Daglis, E. Zesta, G. Balasis, I. R. Mann, C. Katsavrias, and K. Tsinganos (2015), Association of radiation belt electron enhancements with earthward penetration of Pc5 ULF waves: A case study of intense 2001 magnetic storms, *Ann. Geophys.*, *33*, 1431–1442, doi:10.5194/angeo-33-1431-2015.

Glassmeier, K.-H., S. Buchert, U. Motschmann, A. Korth, and A. Pedersen (1999), Concerning the generation of geomagnetic giant pulsations by drift-bounce resonance ring current instabilities, *Ann. Geophys.*, *17*, 338–350, doi:10.1007/s00585-999-0338-4.

Goldstein, J., M. F. Thomsen, and A. DeJong (2014a), In situ signatures of residual plasmaspheric plumes: Observations and simulation, *J. Geophys. Res. Space Physics*, *119*, 4706–4722, doi:10.1002/2014JA019953.

Goldstein, J., S. D. Pascuale, C. Kletzing, W. Kurth, K. J. Genestreti, R. M. Skoug, B. A. Larsen, L. M. Kistler, C. Mouikis, and H. Spence (2014b), Simulation of Van Allen Probes plasmapause encounters, *J. Geophys. Res. Space Physics*, *119*, 7464–7484, doi:10.1002/2014JA020252.

Grubb, R., P. L. Bornmann, G. Heckman, T. Onsager, H. Singer, and R. Viereck (1996), Space environment monitoring mission beyond GOES-M, in *Proceedings of the SPIE, GOES-8 and Beyond*, vol. 2812, edited by E. R. Washwell, pp. 320–328, SPIE-The International Society for Optical Engineering, Bellingham, Wash., doi:10.1117/12.254080.

Hamlin, D. A., R. Karplus, R. C. Vik, and K. M. Watson (1961), Mirror and azimuthal drift frequencies for geomagnetically trapped particles, *J. Geophys. Res.*, *66*, 1–4, doi:10.1029/JZ066i001p00001.

Hasegawa, A. (1969), Drift mirror instability in the magnetosphere, *Phys. Fluids*, *12*(12), 2642–2650, doi:10.1063/1.1692407.

Heckman, G., D. Speich, J. Hirman, and T. DeFoor (1996), NOAA Space Environment Center mission and the GOES space environment monitoring subsystem, in *Proceedings of the SPIE, GOES-8 and Beyond*, vol. 2812, edited by E. R. Washwell, pp. 274–280, SPIE, Denver, Colo., doi:10.1117/12.254074.

Hughes, W. J., D. J. Southwood, B. Mauk, R. L. McPherron, and J. N. Barfield (1978a), Alfven waves generated by an inverted plasma energy distribution, *Nature*, *275*, 43–45, doi:10.1038/275043a0.

Hughes, W. J., R. L. McPherron, and J. N. Barfield (1978b), Geomagnetic pulsations observed simultaneously on three geostationary satellites, *J. Geophys. Res.*, *83*, 1109–1116, doi:10.1029/JA083iA03p01109.

Hughes, W. J., R. L. McPherron, J. N. Barfield, and B. H. Mauk (1979), A compressional Pc4 pulsation observed by three satellites in geostationary orbit near local midnight, *Planet. Space Sci.*, *27*, 821–840, doi:10.1016/0032-0633(79)90010-2.

Kistler, L. M., et al. (2016), The source of O^+ in the storm time ring current, *J. Geophys. Res. Space Physics*, *121*, 5333–5349, doi:10.1002/2015JA022204.

Kivelson, M. G., and D. J. Southwood (1983), Charged particle behavior in low-frequency geomagnetic pulsations. III—Spin phase dependence, *J. Geophys. Res.*, *88*, 174–182, doi:10.1029/JA088iA01p00174.

Kivelson, M. G., and D. J. Southwood (1985), Resonant ULF waves—A new interpretation, *Geophys. Res. Lett.*, *12*, 49–52, doi:10.1029/GL012i001p00049.

Kivelson, M. G., and D. J. Southwood (1986), Coupling of global magnetospheric MHD eigenmodes to field line resonances, *J. Geophys. Res.*, *91*, 4345–4351, doi:10.1029/JA091iA04p04345.

Kletzing, C., et al. (2013), The electric and magnetic field instrument suite and integrated science (EMFISIS) on RBSP, *Space Sci. Rev.*, 1–55, doi:10.1007/s11214-013-9993-6.

Korotova, G. I., et al. (2015), Van Allen Probe observations of drift-bounce resonances with Pc 4 pulsations and wave-particle interactions in the pre-midnight inner magnetosphere, *Ann. Geophys.*, *33*, 955–964, doi:10.5194/angeo-33-955-2015.

Kurth, W. S., S. De Pascuale, J. B. Faden, C. A. Kletzing, G. B. Hospodarsky, S. Thaller, and J. R. Wygant (2015), Electron densities inferred from plasma wave spectra obtained by the Waves instrument on Van Allen Probes, *J. Geophys. Res. Space Physics*, *120*, 904–914, doi:10.1002/2014JA020857.

Lin, N., R. L. McPherron, M. G. Kivelson, and D. J. Williams (1988), An unambiguous determination of the propagation of a compressional Pc 5 wave, *J. Geophys. Res.*, *93*, 5601–5612, doi:10.1029/JA093iA06p05601.

Liu, W., J. B. Cao, X. Li, T. E. Sarris, Q.-G. Zong, M. Hartinger, K. Takahashi, H. Zhang, Q. Q. Shi, and V. Angelopoulos (2013), Poloidal ULF wave observed in the plasmasphere boundary layer, *J. Geophys. Res. Space Physics*, *118*, 4298–4307, doi:10.1002/jgra.50427.

Mauk, B. H., N. J. Fox, S. G. Kanekal, R. L. Kessel, D. G. Sibeck, and A. Ukhorskiy (2013), Science objectives and rationale for the Radiation Belt Storm Probes Mission, *Space Sci. Rev.*, *179*, 3–27, doi:10.1007/s11214-012-9908-y.

Mitchell, D. G., et al. (2013), Radiation Belt Storm Probes Ion Composition Experiment (RBSPICE), *Space Sci. Rev.*, *179*, 263–308, doi:10.1007/s11214-013-9965-x.

Motoba, T., et al. (2015), Link between premidnight second harmonic poloidal waves and auroral undulations: Conjugate observations with a Van Allen Probe spacecraft and a THEMIS all-sky imager, *J. Geophys. Res. Space Physics*, *120*, 1814–1831, doi:10.1002/2014JA020863.

Rae, I. J., I. R. Mann, K. R. Murphy, L. G. Ozeke, D. K. Milling, A. A. Chan, S. R. Elkington, and F. Honary (2012), Ground-based magnetometer determination of in situ Pc4-5 ULF electric field wave spectra as a function of solar wind speed, *J. Geophys. Res.*, *117*, A04221, doi:10.1029/2011JA017335.

Roederer, J. G. (1970), *Dynamics of Geomagnetically Trapped Radiation*, Springer, New York.

Singer, H. J., W. J. Hughes, and C. T. Russell (1982), Standing hydromagnetic waves observed by ISEE 1 and 2—Radial extent and harmonic, *J. Geophys. Res.*, *87*, 3519–3529, doi:10.1029/JA087iA05p03519.

Southwood, D. J. (1976), A general approach to low-frequency instability in the ring current plasma, *J. Geophys. Res.*, *81*(19), 3340–3348, doi:10.1029/JA081i019p03340.

Southwood, D. J., and M. G. Kivelson (1981), Charged particle behavior in low-frequency geomagnetic pulsations. I Transverse waves, *J. Geophys. Res.*, *86*, 5643–5655, doi:10.1029/JA086iA07p05643.

Southwood, D. J., J. W. Dungey, and R. J. Etherington (1969), Bounce resonant interaction between pulsations and trapped particles, *Planet. Space Sci.*, *17*, 349–361, doi:10.1016/0032-0633(69)90068-3.

Spence, H., et al. (2013), Science goals and overview of the Radiation Belt Storm Probes (RBSP) Energetic Particle, Composition, and Thermal Plasma (ECT) suite on NASA's Van Allen Probes Mission, *Space Sci. Rev.*, *179*(1–4), 311–336, doi:10.1007/s11214-013-0007-5.

Su, S.-Y., A. Konradi, and T. A. Fritz (1977), On propagation direction of ring current proton ULF waves observed by ATS 6 at 6.6 R_E, *J. Geophys. Res.*, *82*, 1859–1868, doi:10.1029/JA082i013p01859.

Takahashi, K., and B. J. Anderson (1992), Distribution of ULF energy (f is less than 80 mHz) in the inner magnetosphere—A statistical analysis of AMPTE CCE magnetic field data, *J. Geophys. Res.*, *97*, 10,751–10,773, doi:10.1029/92JA00328.

Takahashi, K., and R. E. Denton (2007), Magnetospheric seismology using multiharmonic toroidal waves observed at geosynchronous orbit, *J. Geophys. Res.*, *112*, A05204, doi:10.1029/2006JA011709.

Takahashi, K., R. W. McEntire, A. T. Y. Lui, and T. A. Potemra (1990), Ion flux oscillations associated with a radially polarized transverse Pc 5 magnetic pulsation, *J. Geophys. Res.*, *95*, 3717–3731, doi:10.1029/JA095iA04p03717.

Takahashi, K., N. Sato, J. Warnecke, H. Luehr, H. E. Spence, and Y. Tonegawa (1992), On the standing wave mode of giant pulsations, *J. Geophys. Res.*, *97*, 10,717–10,732, doi:10.1029/92JA00382.

Takahashi, K., K.-H. Glassmeier, V. Angelopoulos, J. Bonnell, Y. Nishimura, H. J. Singer, and C. T. Russell (2011), Multisatellite observations of a giant pulsation event, *J. Geophys. Res.*, *116*, A11223, doi:10.1029/2011JA016955.

Takahashi, K., M. D. Hartinger, V. Angelopoulos, K.-H. Glassmeier, and H. J. Singer (2013), Multispacecraft observations of fundamental poloidal waves without ground magnetic signatures, *J. Geophys. Res. Space Physics*, *118*, 4319–4334, doi:10.1002/jgra.50405.

Trefethen, L. (2000), *Spectral Methods in MATLAB*, Society for Industrial and Applied Mathematics, Philadelphia, Pa.

Tsyganenko, N. A. (1989), A magnetospheric magnetic field model with a warped tail current sheet, *Planet. Space Sci.*, *37*, 5–20, doi:10.1016/0032-0633(89)90066-4.

Ukhorskiy, A. Y., M. I. Sitnov, K. Takahashi, and B. J. Anderson (2009), Radial transport of radiation belt electrons due to stormtime Pc5 waves, *Ann. Geophys.*, *27*, 2173–2181, doi:10.5194/angeo-27-2173-2009.

Vassiliadis, D., I. R. Mann, S. F. Fung, and X. Shao (2007), Ground Pc3 Pc5 wave power distribution and response to solar wind velocity variations, *Planet. Space Sci.*, *55*, 743–754, doi:10.1016/j.pss.2006.03.012.

Vetoulis, G., and L. Chen (1994), Global structures of Alfven-ballooning modes in magnetospheric plasmas, *Geophys. Res. Lett.*, *21*, 2091–2094, doi:10.1029/94GL01703.

Vetoulis, G., and L. Chen (1996), Kinetic theory of geomagnetic pulsations 3. Global analysis of drift Alfvén-ballooning modes, *J. Geophys. Res.*, *101*, 15,441–15,456, doi:10.1029/96JA00494.

Walker, A. D. M. (1987), Theory of magnetospheric standing hydromagnetic waves with large azimuthal wave number. I—Coupled magnetosonic and Alfven waves, *J. Geophys. Res.*, *92*, 10,039–10,045, doi:10.1029/JA092iA09p10039.

Walker, A. D. M., and H. Pekrides (1996), Theory of magnetospheric standing hydromagnetic waves with large azimuthal wave number 4. Standing waves in the ring current region, *J. Geophys. Res.*, *101*, 27,133–27,148, doi:10.1029/96JA02701.

Wilson, M. E., T. K. Yeoman, L. J. Baddeley, and B. J. Kellet (2006), A statistical investigation of the invariant latitude dependence of unstable magnetospheric ion populations in relation to high m ULF wave generation, *Ann. Geophys.*, *24*, 3027–3040, doi:10.5194/angeo-24-3027-2006.

Wygant, J., et al. (2013), The electric field and waves instruments on the Radiation Belt Storm Probes Mission, *Space Sci. Rev.*, *179*(1–4), 183–220, doi:10.1007/s11214-013-0013-7.

Zhelavskaya, I. S., M. Spasojevic, Y. Y. Shprits, and W. S. Kurth (2016), Automated determination of electron density from electric field measurements on the Van Allen Probes spacecraft, *J. Geophys. Res. Space Physics*, *121*, 4611–4625, doi:10.1002/2015JA022132.

Zhou, X.-Z., Z.-H. Wang, Q.-G. Zong, R. Rankin, M. G. Kivelson, X.-R. Chen, J. B. Blake, J. R. Wygant, and C. A. Kletzing (2016), Charged particle behavior in the growth and damping stages of ultralow frequency waves: Theory and Van Allen Probes observations, *J. Geophys. Res. Space Physics*, *121*, 3254–3263, doi:10.1002/2016JA022447.